LiSBOA: LiDAR Statistical Barnes Objective Analysis for optimal design of LiDAR scans and retrieval of wind statistics. Part II: Applications to LiDAR measurements of wind turbine wakes

Stefano Letizia, Lu Zhan, and Giacomo Valerio Iungo

Wind Fluids and Experiments (WindFluX) Laboratory, Mechanical Engineering Department, The University of Texas at Dallas, 800 W Campbell Rd, 75080 Richardson, TX, USA

Correspondence: Giacomo Valerio Iungo, (valerio.iungo@utdallas.edu)

Abstract. The LiDAR Statistical Barnes Objective Analysis (LiSBOA), presented in Letizia et al. (2020), is a procedure for the optimal design of LiDAR scans and calculation over a Cartesian grid of the statistical moments of the velocity field. LiDAR data collected during a field campaign conducted at a wind farm in complex terrain are analyzed through the LiSBOA for two different tests. For both case studies, the LiSBOA is leveraged for the optimization of the azimuthal step of the LiDAR and the

5   retrieval of mean equivalent velocity and turbulence intensity fields. In the first case, the wake velocity ~~fields~~ statistics of four utility-scale turbines are reconstructed on a 3D grid, showing the capability of the LiSBOA to capture complex flow features, such as high-speed jet around the nacelle and the wake turbulent shear layers. For the second case, the statistics of the wakes generated by four interacting turbines are calculated over a 2D Cartesian grid and compared to the measurements provided by the nacelle-mounted anemometers. Maximum discrepancies as low as 3% for the mean velocity (with respect to the freestream

10   velocity) and turbulence intensity (in absolute terms) endorse the application of the LiSBOA for LiDAR-based wind resource assessment and diagnostic surveys for wind farms.

List of symbols

- x, y, z: streamwise, spanwise, vertical Cartesian coordinates

- t: time

- ρ: air density

- u, v, w: streamwise, spanwise, vertical velocity components

- L: number of realizations/scans

- θ: azimuth angle

- β: elevation angle

- $\Delta\theta$: azimuth-angle resolution

- τ_a: accumulation time

- Δr: gate length

- N_r: number of range gates along the laser per beam

- T: total sampling time

- σ: smoothing parameter

- m: number of iterations

- R_{max}: radius of influence

- $\boldsymbol{\Delta n}$: half-wavelength vector

- $\boldsymbol{\Delta n_0}$: fundamental half-wavelength vector

- Δd: random data spacing

- $\boldsymbol{dx}$: resolution vector in Cartesian coordinates

- D^m: response at the m-th iteration

- ϵ^I: cost function I (data loss)

- ϵ^{II}: cost function II (standard deviation of the sample mean)

- τ: integral time-scale

- $\tilde{\cdot}$: spatial variable in the scaled frame of reference

- D: rotor diameter

- U_{norm}: 10-minute-averaged normalized density-corrected hub-height wind speed

- P_{norm}: 10-minute-averaged normalized active power

40 - U_{∞}: 10-minute-averaged undisturbed incoming wind speed

- U_{SCADA}: 10-minute-averaged hub-height wind speed

- $U_{\mathrm{SD,\,SCADA}}$: 10-minute-based hub-height standard deviation of wind speed

- TI_{SCADA}: 10-minute-based hub-height turbulence intensity

- U_{met}: 10-minute-averaged wind speed from met tower

45 - L_{O}: Obukhov length

1 Introduction

The use of Doppler light detection and ranging (LiDAR) technology for wind energy applications has largely increased over the last decade (Clifton et al., 2018; Veers et al., 2019). Thanks to the achieved measurement accuracy, simpler and cost-effective deployments compared to traditional met-tower instrumentation, this remote sensing technique is now included in the inter-

50 national standards as a reliable tool for performance diagnostic of wind turbines and wind resource assessment (International Electrotechnical Commission 61400-12-1, 2017). Nonetheless, due to the limited spatio-temporal resolution and the distribution of the sample points in a spherical reference frame, the reconstruction of wind statistics from LiDAR samples still presents several challenges (Sathe et al., 2011; Newman et al., 2016).

In the companion paper (Letizia et al., 2020), we presented a revisited Barnes objective analysis (Barnes, 1964) for the

55 calculation of wind statistics from scattered LiDAR data, which is referred to as LiDAR Statistical Barnes Objective Analysis (LiSBOA). This procedure enables the estimation over a Cartesian grid of the mean, variance and even higher-order central statistical moments of the radial velocity field probed by a scanning Doppler pulsed wind LiDAR. The LiSBOA ~~performs also~~ also performs adequate filtering of small-scale variability in the mean velocity field and mitigation of the dispersive stresses on the higher-order statistics provided that the algorithm is tuned based on the characteristics of the flow under investigation and

60 the ~~data collection strategy is~~ free parameters of the LiDAR scan are optimally designed through the LiSBOA.

The LiSBOA capability to estimate statistics of an ergodic turbulent velocity field makes it a suitable tool for the analysis of wind turbine wakes and the resource assessment of sites characterized by heterogeneous wind conditions, such as in presence of flow distortions induced by complex terrain. Over the last decade, wind LiDARs have been used to investigate wind turbine wakes; for instance, Käsler et al. (2010) and Clive et al. (2011) measured the velocity deficit past utility-scale wind

65 turbines, while Bingöl et al. (2010) used a nacelle-mounted LiDAR to detect wake displacements and validate the dynamic wake meandering model (Larsen et al., 2008). Fitting of the wake velocity deficit was successfully exploited to extract quantitative information about wake evolution from LiDAR measurements (Aitken and Lundquist, 2014; Wang and Barthelmie, 2015; Kumer et al., 2015; Trujillo et al., 2016; Bodini et al., 2017).

A deeper understanding ~~on~~ of the physics of turbine wakes was achieved by calculating temporal (Trujillo et al., 2011; Iungo

70 et al., 2013b; Iungo and Porté-Agel, 2014; Kumer et al., 2015; Machefaux et al., 2015; Van Dooren et al., 2016) or conditional (Aubrun et al., 2016; Machefaux et al., 2016; Garcia et al., 2017; Bromm et al., 2018; Iungo et al., 2018; Zhan et al., 2019, 2020) statistics of the velocity collected through LiDAR scans performed at different times. Using this approach, Iungo and Porté-Agel (2014) detected a significant dependence of the wake recovery rate on atmospheric stability based on time-averaged volumetric LiDAR scans. The same concept was expanded by other authors using ensemble statistics (Machefaux et al., 2016;

75 Carbajo Fuertes et al., 2018; Zhan et al., 2019, 2020). Kumer et al. (2015) carried out a comparison between instantaneous, 10 minutes and daily-averaged velocity and turbulence intensity fields around utility-scale wind turbines, highlighting the presence of persistent turbulent wakes. Trujillo et al. (2011) used a nacelle-mounted LiDAR to quantify meandering-induced wake diffusion and added turbulence from statistics calculated over 10-minute periods.

Second-order statistics are of great interest in wind energy. Iungo et al. (2013b) used velocity time-series extracted from LiDAR fixed scans performed downstream of a 2-MW wind turbine to detect enhanced turbulence intensity in the proximity of the wake shear layers. More recently, temporal statistics over 30-minute periods allowed for the identification of turbulent wake shear layers from both numerical (Fuertes Carbajo and Porté-Agel, 2018) and experimental (Carbajo Fuertes et al., 2018) velocity fields. Aubrun et al. (2016) attempted to characterize the turbulence intensity using bin statistics, even though achieving values higher than expected, i.e. larger than 50%. Zhan et al. (2019) used clustered data of wake velocity fields to retrieve a proxy for the standard deviation of wind speed in the wake of utility-scale turbines. These authors reported significant variability in the wake turbulent statistics depending on the atmospheric stability regime and operative conditions of the wind turbines.

For the above-mentioned technical features of LiDARs, these remote sensing instruments are now also used for wind resource assessment (Liu et al., 2019) enabling estimates of wind statistics for broad ranges of wind conditions and site typology, such as for flat terrains (Karagali et al., 2018; Sommerfeld et al., 2019; Sanchez-Gomez and Lundquist, 2019), complex terrains (Krishnamurthy et al., 2011, 2013; Pauscher et al., 2016; Kim et al., 2016; Vasiljević et al., 2017; Karagali et al., 2018; Risan et al., 2018; Menke et al., 2019; Fernando et al., 2019), near-shore (Hsuan et al., 2014; Floors et al., 2016; Shimada et al., 2018) and off-shore locations (Pichugina et al., 2012; Koch et al., 2014; Gottschall et al., 2018; Viselli et al., 2019). LiDAR scanning strategies for wind resource assessment encompass Doppler beam swinging (DBS) (Hsuan et al., 2014; Pauscher et al., 2016; Kim et al., 2016; Shimada et al., 2018; Gottschall et al., 2018; Viselli et al., 2019; Sommerfeld et al., 2019; Sanchez-Gomez and Lundquist, 2019), Plan Position Indicator (PPI) scans (Krishnamurthy et al., 2011, 2013; Pauscher et al., 2016; Floors et al., 2016; Vasiljević et al., 2017; Karagali et al., 2018), Range Height Indicator (RHI) scans (Pichugina et al., 2012; Floors et al., 2016; Menke et al., 2019; Fernando et al., 2019) or fixed scans (Risan et al., 2018). Statistics are generally calculated based on the canonical 10-minute periods assuming steady inflow conditions, while linear interpolation is widely used for data post-processing.

In the light of great relevance for the wind energy applications of the statistical analysis of wind LiDAR data, for this work, the LiSBOA procedure is applied to ~~virtual and~~ real LiDAR measurements of wind turbine wakes. The scope of this study is dual: first, assessing the capabilities provided by the LiSBOA for the optimal ~~design of the LiDAR scanning strategy~~ selection of the angular step of the LiDAR scans by maximizing the statistical accuracy of the measurements and coverage of the sampling domain with the prescribed spatial resolution; second, showing the potential of the LiSBOA to reconstruct mean velocity and turbulence intensity fields from LiDAR data to unveil important flow features of wind turbine wakes.

With these aims, real LiDAR data collected in the wakes generated by four 1.5-MW wind turbines are analyzed through the LiSBOA. Specific wake features, such as the high-speed jet around the nacelle and the turbulent shear layers, as well as perturbations induced by the complex topography, are detected. Then, to provide a quantitative comparison with the data retrieved ~~by means of~~ through traditional anemometers, the LiSBOA is employed to calculate mean velocity and turbulence intensity fields of the wakes generated by four 1-MW turbines interacting with each other.

The remainder of the manuscript is organized as follows: Sect. 2 provides a description of the site and the experimental setup of the field campaign. In Sect. 3, the scan design and the reconstruction of the statistics of the non-interacting wakes

are discussed, while Sect. 4 presents the results of the comparison between nacelle anemometer statistics and LiSBOA for the
multiple interacting wakes. Finally, conclusions are drawn in Sect. 5. The paper uses symbols introduced in the companion
paper Letizia et al. (2020), which the reader is encouraged to review for a better understanding of the present manuscript.

2   Site description and experimental setup

LiDAR data collected during an experimental campaign carried out at an onshore wind farm are used to assess the potential
of the LiSBOA algorithm for wind energy applications. The measurements were collected during a long-term experimental
campaign conducted at a large wind farm located in North-East Colorado (Fig. 1). This wind park encompasses 221 Mitsubishi
1-MW and 53 General Electric 1.5-MW wind turbines. More technical specifications of the wind turbines are provided in Table
1.

The wind rose, based on 3 years of wind speed and direction measured by the two meteorological (met) towers present on
the site, reveals a prevalence of north-westerly and south-easterly wind directions. A characteristic of this site is the presence
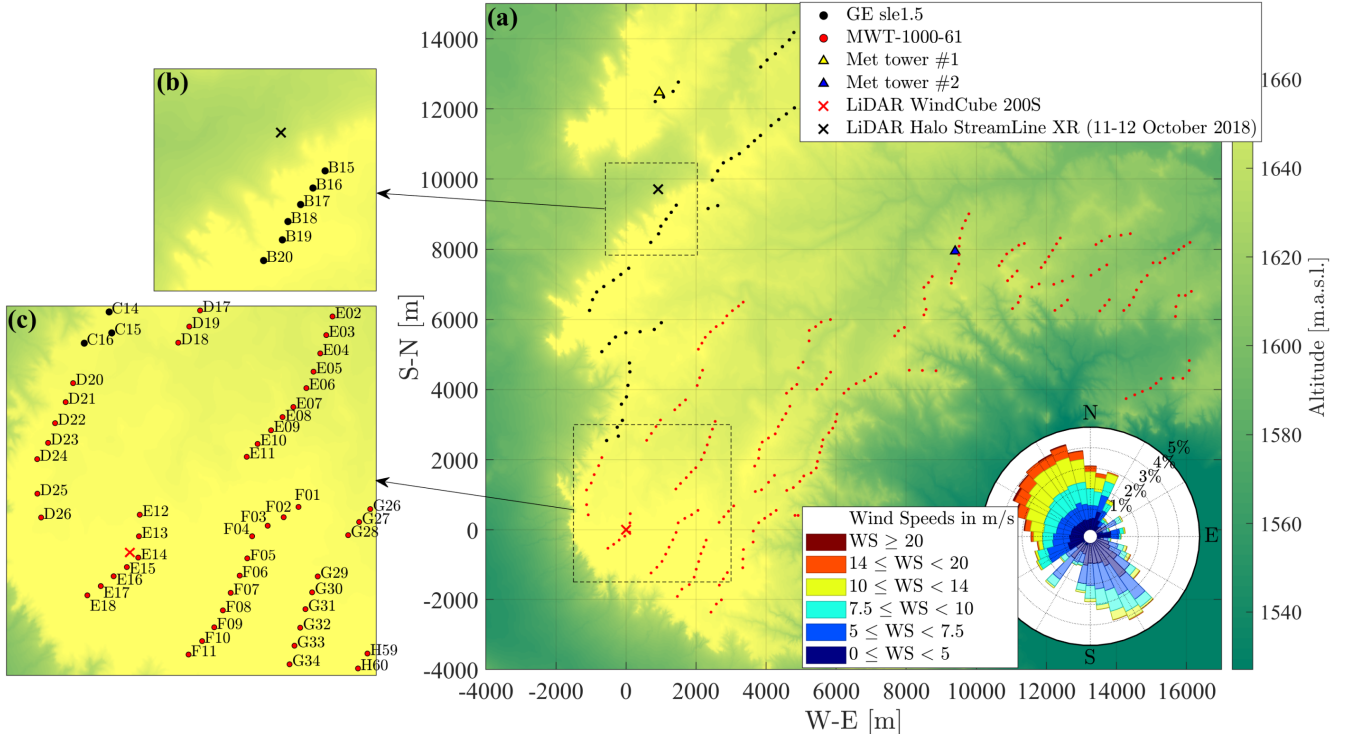
Figure 1. Map of the wind farm under investigation: **(a)** top view of the wind farm, with the diameter of the dots representing the turbine
rotor diameter (in the wind rose, the sectors where both met-towers are potentially affected by turbine wakes are displayed in lighter color);
(b) area probed through Streamline XR LiDAR on 11 and 12 October 2018; **(c)** typical field of view of the Windcube 200S LiDAR.

Table 1. Technical specifications of the wind turbines under investigation.

	MWT-1000-61	GE sle1.5
Rated power [kW]	1000	1500
Cut-in wind speed [m s^{-1}]	3.5	3.5
Cut-out wind speed [m s^{-1}]	25	25
Rated wind speed [m s^{-1}]	13.5	14
Type	Variable pitch/fixed speed	Variable pitch/variable speed
Hub height [m]	69	80
Rotor diameter [m]	61.4	77

Figure 2. Photos of the LiDAR experiment: **(a)** LiDAR Windcube 200S and sonic anemometers Campbell Scientific CSAT3; **(b)** LiDAR Streamline XR; **(c)** GE 1.5sle turbines of the B row.

125 of a steep escarpment with an average jump in altitude of about 80 m surrounding a relatively flat plateau where the turbines are installed.

Two pulsed Doppler scanning wind LiDARs were deployed: a Windcube 200S manufactured by Leosphere (Fig. 2a) was installed for the period May-December 2018 in the southern part of the farm with the scope of detecting turbine wakes and flow distortions induced by the topography. The LiDAR was connected to the UTD mobile LiDAR station (El-Asha et al., 2017;

130 Zhan et al., 2019) for remote control, scan setup, and data acquisition. Furthermore, a StreamLine XR by Halo-Photonics (Fig. 2b) was deployed for the period 11-19 October 2018 at specific sectors to investigate wake interactions and topography-related flow features. Additional details about the LiDARs, including the settings adopted for the present study, are provided in Table 2.

The atmospheric stability is characterized through the Obukhov length (Monin and Obukhov, 1959) retrieved by two CSAT3

135 three-dimensional sonic anemometers manufactured by Campbell Scientific, which were deployed in the proximity of the UTD mobile LiDAR station at 1.4 m and 2.8 m above the ground. Two met-towers are installed in the northern part of the park, as shown in Fig. 1. Each tower is equipped with 4 anemometers installed in paired configuration at heights of 50 m and 80

Table 2. Technical specifications and settings of the wind LiDARs deployed during the field campaign.

	WindCube 200S	StreamLine XR
Type	Pulsed - scanning	Pulsed - scanning
Scanning mode	Continuous	Step-stare
Wavelength [nm]	1543	1500
Pulse length [ns]	200	200
Frequency [kHz]	20	10
Gate length [m]	50	18
Number of gates	80	200
Rotation speed [° s^{-1}]	1	0.85
Detection range [m s^{-1}]	± 30	± 20

m for met tower #1, and 50 m and 69 m for met tower #2. Mean and standard deviation of wind speed and direction are stored every 10 minutes, along with the mean temperature and barometric pressure. In the present work, wind velocity data at each height are corrected for the flow distortion due to the tower following the guidelines provided by the IEC standards (International Electrotechnical Commission 61400-12-1 (2017) Annex G). Additionally, mean and standard deviation over 10-minute periods of nacelle wind speed, power, RPM, and blade pitch, collected and stored by the supervisory control and data acquisition (SCADA) system were made available. Normalized average power, P_{norm}, and C_p curves based on the nacelle anemometers are built by leveraging data for the period 2016-2018, and shown in Fig. 3 as a function of the density-corrected normalized wind speed (International Electrotechnical Commission 61400-12-1, 2017):

$$U_{\mathrm{norm}} = \frac{U_{\mathrm{SCADA}}}{U_{\mathrm{rated}}} \cdot \left(\frac{\rho_{\mathrm{met}}}{\rho_{\mathrm{ref}}} \right)^{1/3}, \tag{1}$$

where $\rho_{\mathrm{ref}} = 1.225$ Kg m^{-3} is the reference density at the sea level, U_{SCADA} is the 10-minute average of the wind speed measured by the nacelle-mounted anemometers, while the local air density ρ_{met} is calculated from the meteorological data according to the international standard (International Electrotechnical Commission 61400-12-1, 2017). Another important parameter derived form the SCADA data is the turbulence intensity at the rotor, defined as:

$$TI_{\mathrm{SCADA}} = \frac{U_{\mathrm{SD, SCADA}}}{U_{\mathrm{SCADA}}} \tag{2}$$

where $U_{\mathrm{SD,SCADA}}$ is the standard deviation of wind speed over 10-minute periods.

The two LiDARs performed a great variety of scans during the campaign, based on the specific phenomena under investigation. For the present analysis, we focus on the 3D reconstruction of non-interacting wakes using the high-resolution data collected with the Halo Streamline XR LiDAR and the 2D reconstruction of multiple overlapping wakes detected by the Windcube 200S.
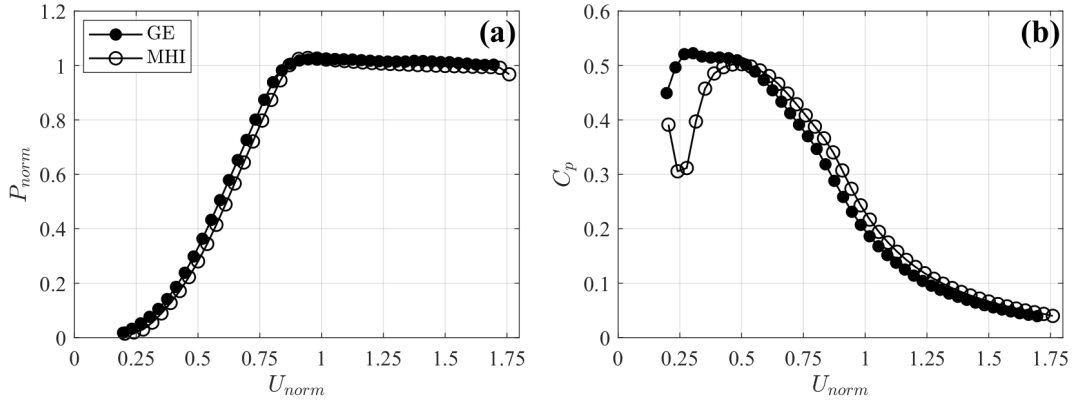
Figure 3. Performance curves for the General Electric and Mitsubishi wind turbines: **(a)** normalized power, P_{norm}; **(b)** power coefficient, C_p.

3   Application of the LiSBOA to volumetric LiDAR data

The present section aims to explore the potential of the LiSBOA for the ~~optimal design~~ selection of the optimal azimuthal resolution of a LiDAR ~~experiment~~scan, data post-processing, and reconstruction of 3D flow statistics. The dataset used in this section was collected on 11 October 2018 over the farm region shown in Fig. 1b through a StreamLine XR LiDAR. The goal of the experiment is to investigate the evolution of multiple turbine wakes advected over complex terrain. Figure 4 shows the site of the deployment and the relative distances between the LiDAR and the turbine hubs.

The deployment location was chosen to scan the wakes generated by the wind turbines B16-B19 for south-south-east wind directions. The LiDAR was deployed off a county road that connects the plateau with the surrounding plains, with a consequent difference in altitude between the instrument and the base of the turbines of about 40 m. To probe the wake region of turbines B16-B19 (Fig. 2b) and the leeward side of the ridge, seven PPI scans were performed by sweeping an azimuthal range of 65° with elevations angles, β, set to 5°, 6°, 7°, 8°, 10°, 12° and 15°. The total sampling time was selected equal to ~~$T = 1h$~~$T = 1$ h, since the local weather forecast service provided by the wind farm operator predicted one hour of steady wind conditions

Figure 4. Satellite map of deployment of Halo StreamLine XR on October 11 2018. Source: Google Maps.

blowing with SSE mean direction and speed of $U_\infty \approx 6$ m s^{-1}. The aerosol concentration allowed for the selection of a gate

170 length of $\Delta r = 18$ m and accumulation time of 1.2 s.

As reported in Sect. 4 of Letizia et al. (2020), several parameters of the flow under investigation are required for the optimal design of the LiDAR scans. The fundamental half-wavelengths typical for wind turbine wakes were selected equal to those used in Sect. 5 of Letizia et al. (2020), i.e. $\Delta n_{0,x} = 2.5D$, $\Delta n_{0,y} = \Delta n_{0,z} = 0.5D$. Similarly, the integral time-scale was chosen equal to $\tau U_\infty / D = 0.4$ ($\tau \sim 5$ s). Finally, a measurement volume with dimensions of 1,000 m, 950 m, 130 m in the

175 streamwise, transverse, and vertical directions, respectively, was selected to probe wakes generated from the turbines B16-B19 and the downwind region of the escarpment. The expected characteristic velocity standard deviation was estimated to be $\sqrt{\overline{u'^2}} = 0.125\, U_\infty$ based on previous field measurements of turbine wakes under stable conditions (Zhan et al., 2019).

For the selection of the optimal azimuthal angular resolution of the LiDAR scan, the LiSBOA is applied to produce a Pareto front for six possible angular resolutions, $\Delta\theta$, between 0.25° and 4°, and four values of the smoothing parameter,

180 $\sigma = [1/4, 1/6, 1/8, 1/17]$. As shown in Fig. 5, the optimal LiDAR scan is that with angular resolution $\Delta\theta = 1°$ and $\sigma = 1/4$ or $\sigma = 1/6$. Generally, an increasing $\Delta\theta$ entails a reduction of the standard deviation of the mean, ϵ^{II}, yet values higher than $\Delta\theta = 1°$ do not lead to significant reductions of ϵ^{II} while worsening the data loss, ϵ^I, indicating a larger number of grid points not satisfying the Petersen-Middleton constraint.

In Fig. 5, the values of the cost function ϵ^I and ϵ^{II} calculated from the LiDAR data after the quality-control process (Beck

185 and Kühn, 2017) are also reported for the optimal angular spacing of the LiDAR $\Delta\theta = 1°$. It is noteworthy that there is
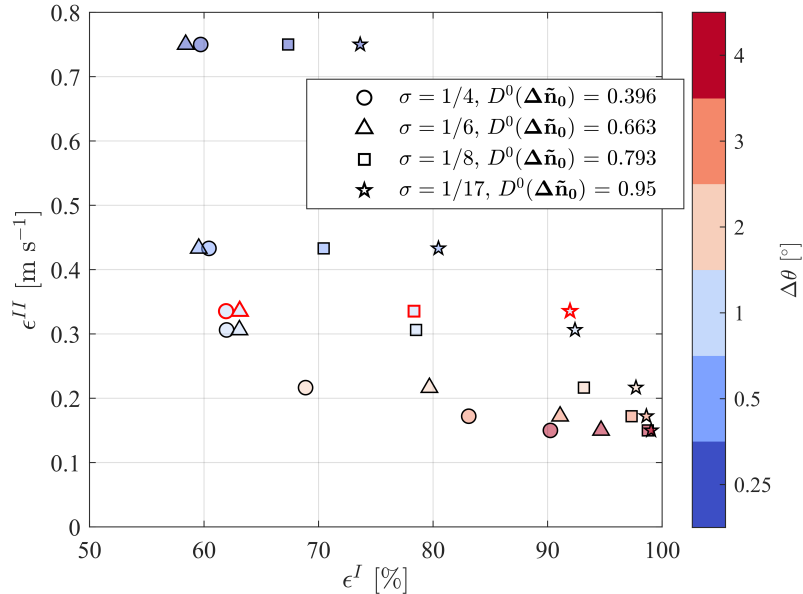
Figure 5. Pareto front for the design of the optimal LiDAR scan for the reconstruction of the wakes generated by the wind turbines B16-B19. The markers highlighted in red correspond to the respective parameters obtained from the actual LiDAR data after the quality control process.

negligible difference between the values calculated before and after the quality control of the LiDAR data, indicating that the data loss due to the acquisition error is negligible in the domain of interest. The spatial distributions of the grid points satisfying the Petersen-Middleton constraint for different values of $\Delta\theta$ and $\sigma = 1/4$ are reported in Fig. 6. It can be observed as $\Delta\theta = 1°$ represents the highest angular step ensuring an acceptable coverage of the spatial domain.

190   The data collected adopting the optimal scanning strategy with $\Delta\theta = 1°$ are now post-processed to calculate mean streamwise velocity and turbulence intensity. The time series of wind speed and direction recorded by the sensors installed on the met tower #1 at hub height and located at a distance of 2,700 m in the north direction from the test site are leveraged to characterize the incoming wind. The evolution of wind speed and direction along with the velocity field measured with three specific PPI
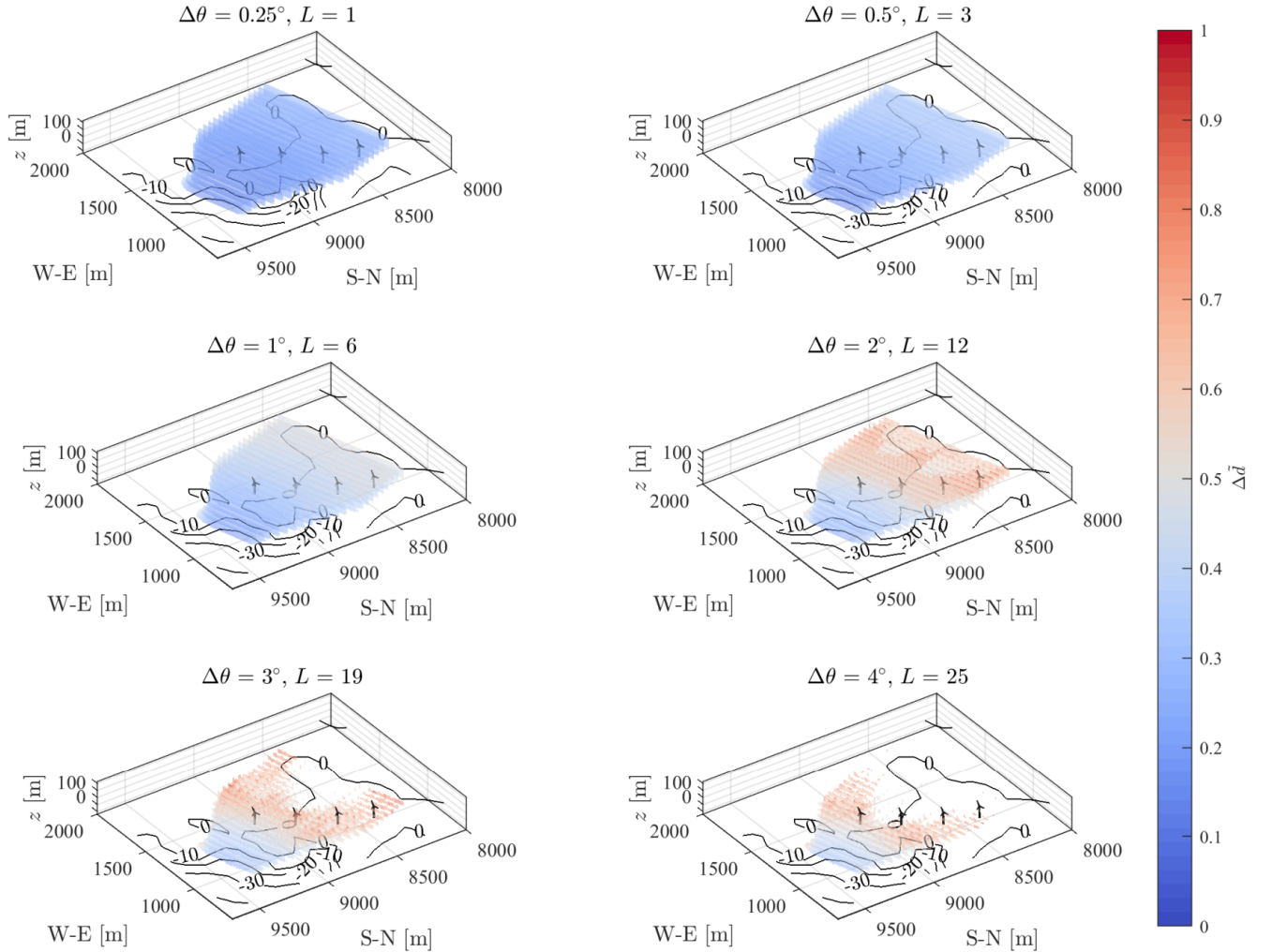
Figure 6. Random data spacing, $\Delta\tilde{d}$, for 6 volumetric scans with different angular resolution and $\sigma = 1/4$. Points violating the Petersen-Middleton constraint ($\Delta\tilde{d} > 1$) are not displayed.

scans are reported in Fig. 7. For the ~~time~~ period between 20:30 and 21:30 local time (MDT) and indicated by the shaded area in Figs. 7a and b, the wind speed remained within the range between 5.1 m s^{-1} and 7.1 m s^{-1}, while the wind direction departed less than 10° from its mean value of $\overline{\theta}_w = 163.4°$. The wind and power data, which are recorded by the SCADA (Fig. 8), confirms that the turbines experienced fairly homogeneous inflow conditions, with differences in power capture 5% smaller than the rated value. The values of normalized velocity together with the performance curves (Fig. 3) indicate that the turbines were operating in region II of the power curve for the whole interval of interest.

Since statistical stationarity is an important assumption for the LiSBOA applications, adequate post-processing of the LiDAR data is needed to avoid effects on the reconstructed flow statistics due to the wind variability. Specifically, the wind speed variability is corrected by making the line-of-sight velocity non-dimensional with the incoming wind speed. To this aim, the instantaneous velocity field measured by the LiDAR is divided by the synchronized mean wind speed obtained from the met tower #1, as explained above. Furthermore, scans performed when the wind direction was outside of the range $\overline{\theta}_w \pm \Delta\theta_w/2$, with $\Delta\theta_w = 10°$, are excluded. After the quality control based on the dynamic filtering (Beck and Kühn, 2017), 169,000 data points out of 455,000 are made available for the LiSBOA reconstruction on a Cartesian grid with resolution equal to
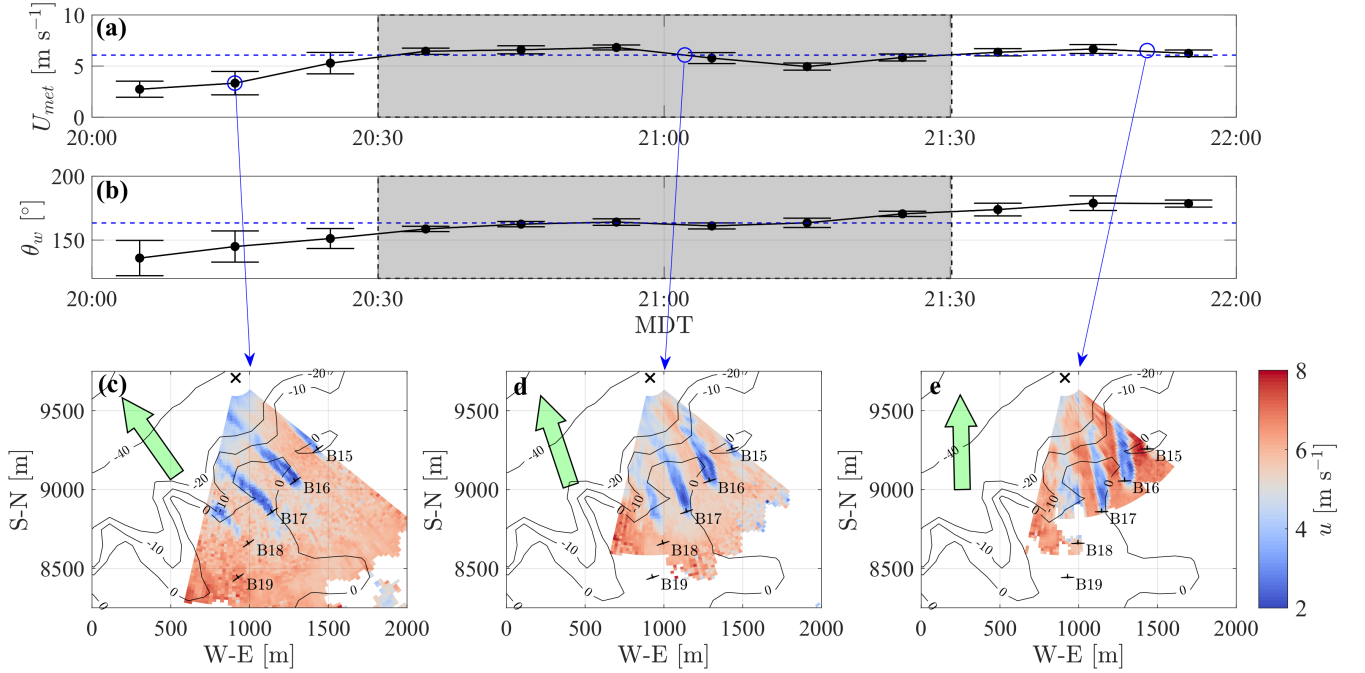
Figure 7. 3D LiDAR scans of five wind turbines: **(a)** 10-minute average wind speed measured from the anemometers installed at 50-m and 80-m height on the met-tower #1; the error bar represents the standard deviation over 10 minutes; the shaded area represents the interval selected for the LiSBOA application; **(b)** 10-minute average wind direction in geophysical reference system measured from the vanes installed at 50 m and 80 m on met-tower #1; **(c)**, **(d)** and **(e)** equivalent velocity fields measured with PPI scans at different times; the green arrow is oriented as the mean wind direction measured by the met-tower #1, while the black cross indicates the LiDAR location.
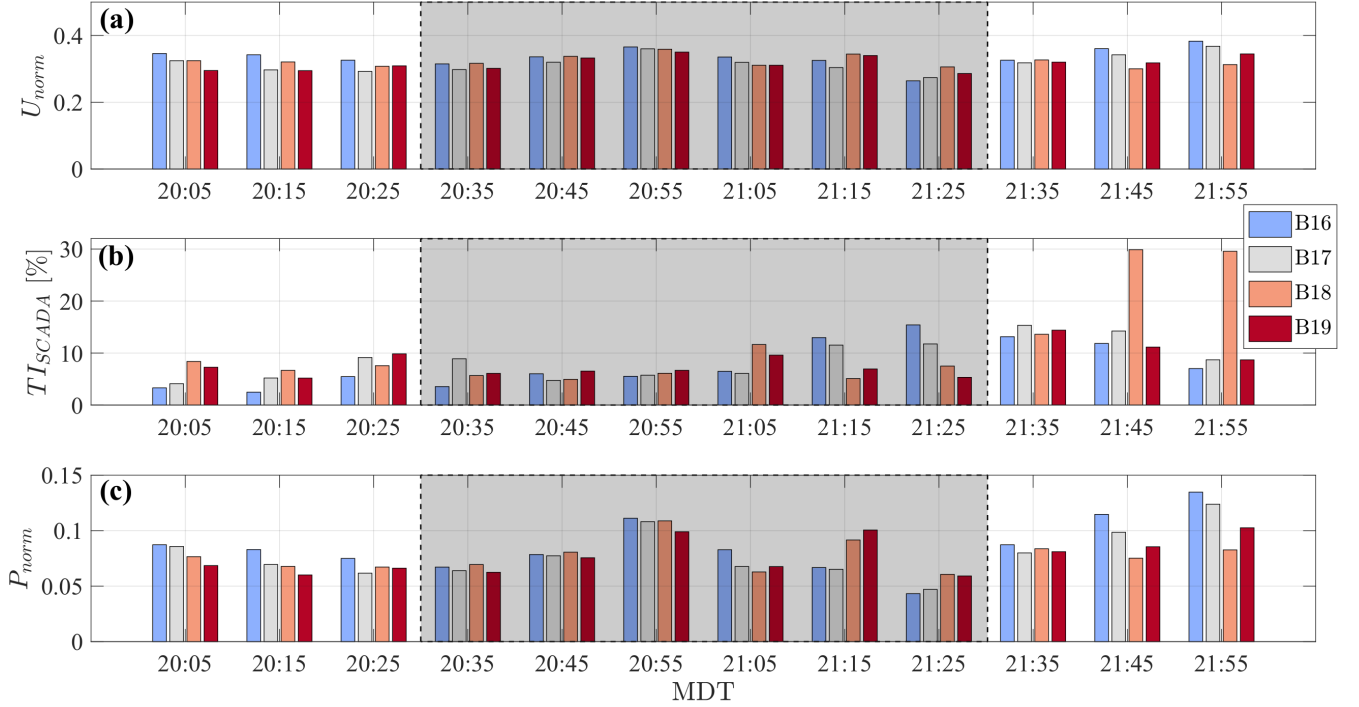
Figure 8. SCADA data during the selected testing period: **(a)** normalized hub-height velocity; **(b)** turbulence intensity; **(c)** normalized power.

$dx = 0.25\mathbf{\Delta n_0}$. Isolated grid regions violating the Middleton-Petersen constraint ($< 2\%$ of the total number of grid points) are rejected and their respective values are ~~interpolated~~ _filled_ through Laplacian interpolation (*inpaint_nans.m* in Matlab). This analysis is restricted to the streamwise component of the wind velocity, which is estimated using the equivalent velocity approach (Zhan et al., 2019). The non-dimensional equivalent velocity is referred to as $\overline{u}/U_\infty$ in the remainder of the paper, while the associated turbulence intensity is referred to as $\sqrt{\overline{u'^2}}/\overline{u}$.

Figures 9 and 10 show 3D renderings of the non-dimensional velocity and turbulence intensity fields obtained by using the parameters $\sigma = 1/4$ - $m = 5$. Wake features, such as turbulent diffusion, the high-momentum jet in the hub region and the turbulent shear layer at the wake boundary, are well-captured. Two highly turbulent regions are located on both sides of the wakes, which is a distinctive signature of wake meandering occurring mostly horizontally in the ABL (España et al., 2011). The lack of symmetry and similarity among different turbines, however, suggests that full statistical convergence is not achieved on the second-order statistics for the available dataset. The low-speed region hovering over the down-slope represents most probably the upper part of the low momentum zone that occurs past sharp escarpments (Berg et al., 2011).

The effect of the combination $\sigma - m$ on higher-order statistics is investigated by extracting the turbulence intensity at different cross-stream planes. The optimal pairs $\sigma - m$ identified by the Pareto front analysis (Fig. 5), viz. $\sigma = 1/4$ - $m = 5$ and $\sigma = 1/6$ - $m = 2$, are tested here. One may expect that due to the difference in the response of the high-order moments of the fundamental mode between the two pairs, $D^0(\mathbf{\Delta \tilde{n}_0})$, the first case would exhibit a significantly lower $\sqrt{\overline{u'^2}}/\overline{u}$ with respect to the second
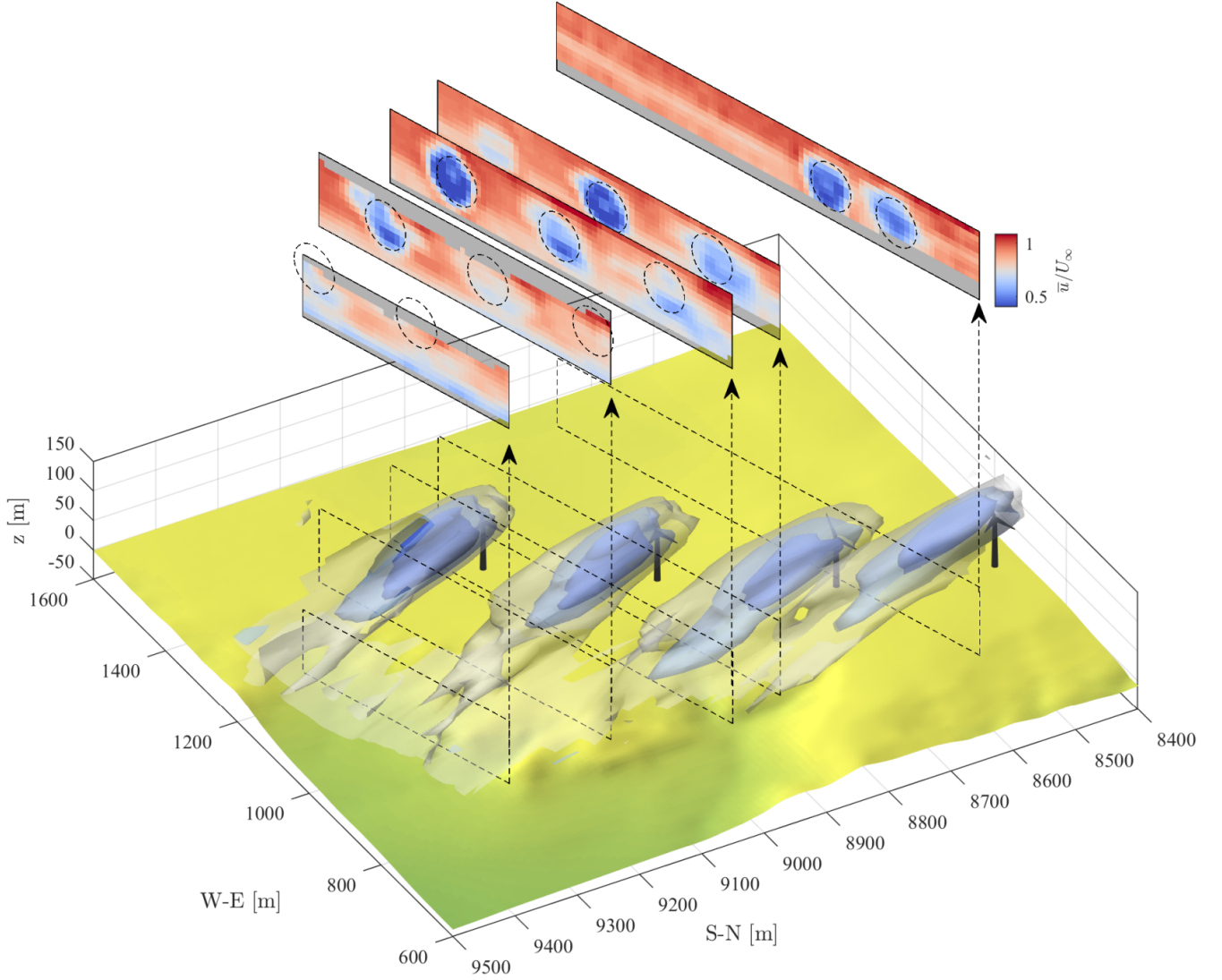
Figure 9. 3D rendering of the normalized mean equivalent velocity field reconstructed with $\Delta\theta_w = 10°$. The three isosurfaces represent $\overline{u}/U_\infty = 0.45$, 0.6 and 0.75, while the color maps represent cross-sections of the mean velocity field over the respective planes reported in the rendering. The dashed circles correspond to the rotor swept area of turbines B16-B19 (from left to right) projected onto the specific cross-plane.

one. However, as shown in Fig. 11, the peaks of turbulence intensity are quite similar between the two cases. The main difference between the two reconstruction processes is a smoother distribution of $\sqrt{\overline{u'^2}}/\overline{u}$ for $\sigma = 1/4 - m = 5$. The similarity between the two cases is due essentially to two reasons: first, the smallest energy-containing length scales of the turbulence intensity field (i.e. shear layer thickness) are larger than the selected fundamental mode $\Delta n_{0,y} = \Delta n_{0,z} = 0.5D$; second, the
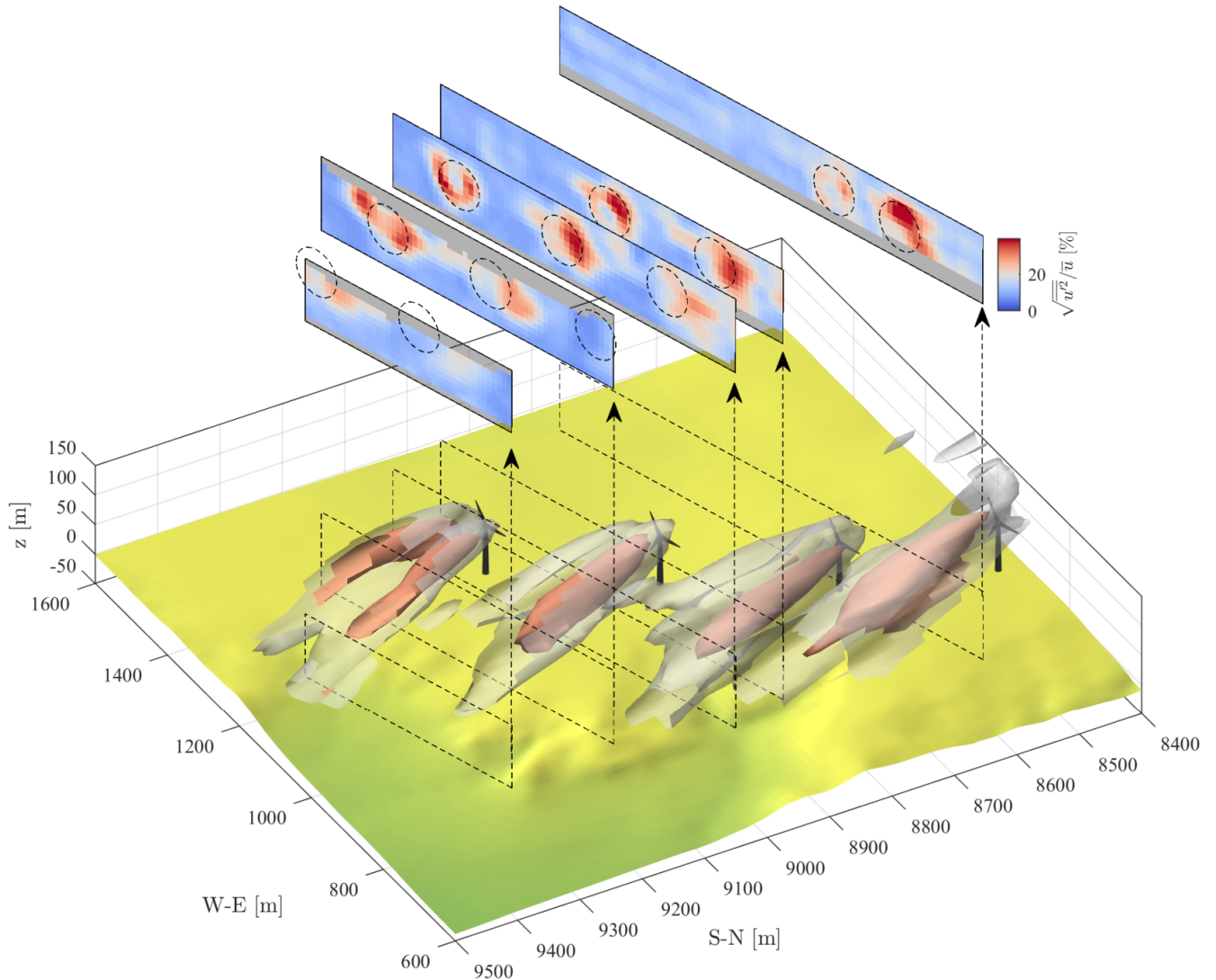
Figure 10. 3D rendering of the turbulence intensity field reconstructed with $\Delta\theta_w = 10°$. The two isosurfaces represent $\sqrt{\overline{u'^2}}/\overline{u} =$ levels of 20% and 30%, while the color maps represent cross-sections of the turbulence intensity field over the respective planes reported in the rendering. The dashed circles correspond to the rotor swept area of turbines B16-B19 (from left to right) projected onto the specific cross-plane.

larger number of points per grid node averaged for the $\sigma = 1/4$ case, leads to a higher variance due to the reduction of the bias of the estimator of the variance, which partially compensates the lower theoretical response. Summarizing, this sensitivity analysis suggests that the choice of the $\sigma - m$ pair cannot be based purely on the theoretical response, since it does not take into account non-ideal effects deriving from the discrete and non-uniform data distribution. Instead, an a posteriori analysis of the statistics retrieved is recommended to select the best $\sigma - m$ values.

230
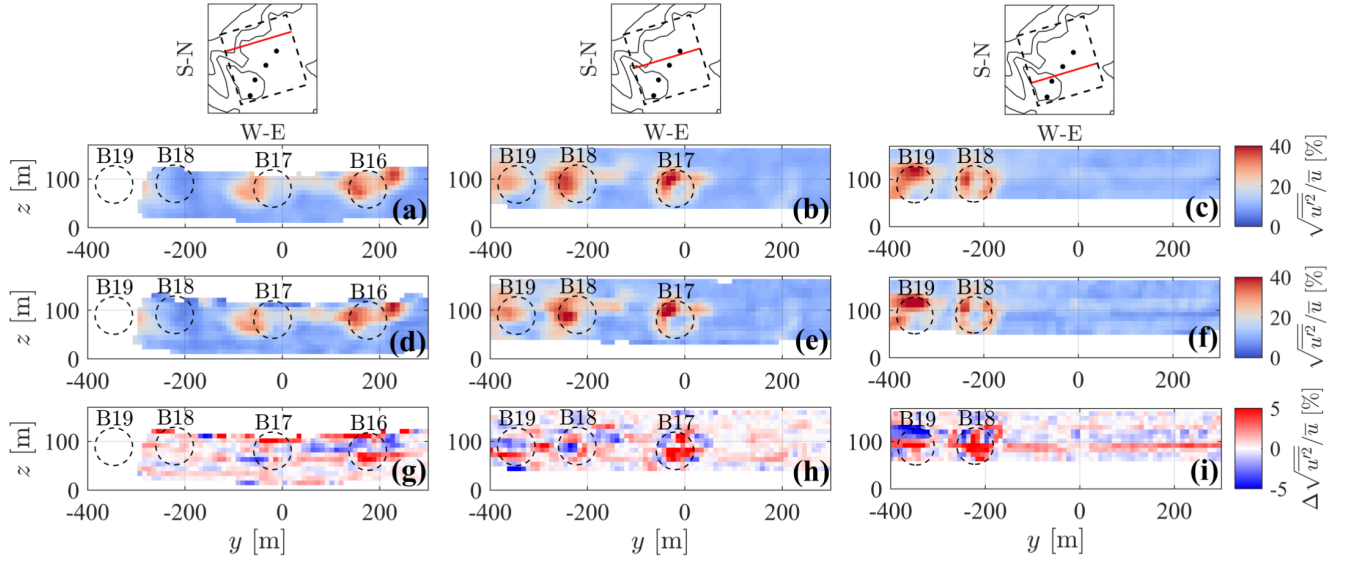
Figure 11. Comparison of the turbulence intensity reconstructed with $\sigma = 1/4 - m = 5$ **(a, b, c)** vs. $\sigma = 1/6 - m = 2$ **(d, e, f)** and their difference **(g, h, i)** for three selected streamwise locations indicated by the red lines in the top maps.
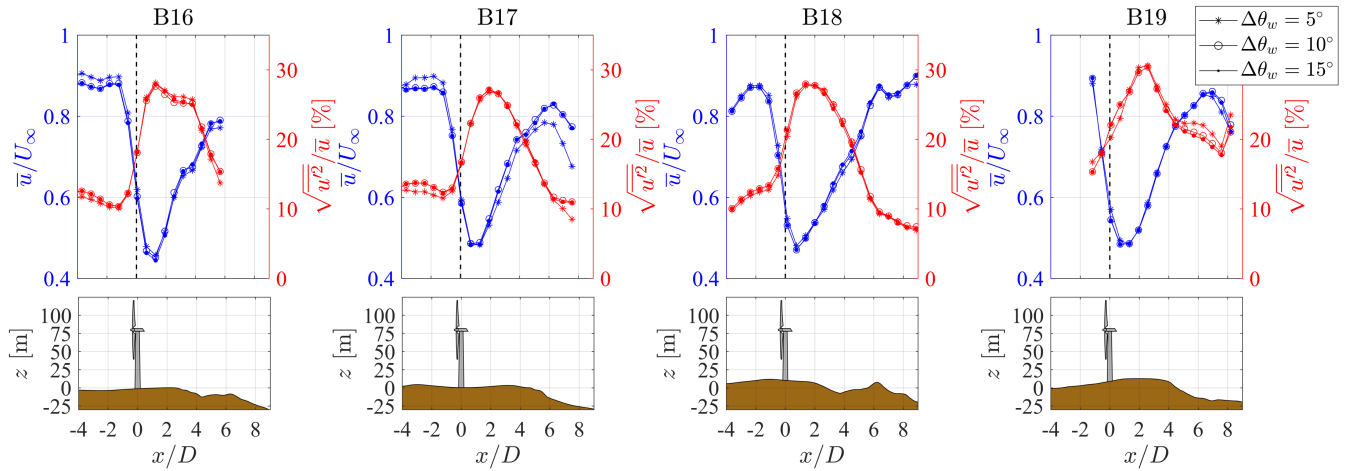
Figure 12. Rotor-averaged streamwise mean velocity and turbulence intensity as a function of the downstream distance from the turbine and associated altitude profile.

Turbine-wake statistics are extremely sensitive to the width of the selected wind sector (Barthelmie et al., 2009; Hansen and Barthelmie, 2014). It is well-known that widening the wind direction range can lead to an enhanced wake diffusion and turbulence intensity (Trujillo et al., 2011; Kumer et al., 2015), compensated by higher data availability and statistical significance. A sensitivity analysis to the wind sector width for reconstructing the statistics through the LiSBOA for two

additional values of $\Delta\theta_w$ is now presented. Besides the baseline value of $10°$, effects of a narrower ($\Delta\theta_w = 5°$) and wider ($\Delta\theta_w = 15°$) range are investigated. The standard deviation of the wind direction associated with the different sectors is $1.08°$, $1.93°$ and $2.74°$ for $\Delta\theta_w = 5°, 10°, 15°$, respectively. Figure 12 shows the rotor-averaged velocity and turbulence intensity for each turbine as a function of the downstream distance from the rotor. The profiles of the mean and standard deviation obtained for different $\Delta\theta_w$ are practically the same, indicating that the effects of wind direction variability on wake flow statistics are not significant. For the sake of completeness, the velocity and turbulence intensity sampled in the cross-stream plane where the maximum velocity deficit occurs ($x/D \sim 1.3$) for all the turbines and the $\Delta\theta_w$ are shown in Fig. 13. The discrepancies due to different $\Delta\theta_w$ are negligible. A more evident mismatch can be observed in the shape of the wakes among different wind turbines, with the wake of turbine B19, in particular, showing the velocity deficit and turbulence peak that are displaced above the hub height. Turbine B19 is also the only one facing a slightly inclined terrain (see Fig. 12), which may have caused a skewed inflow.

4   Application of the LiSBOA to interacting wind turbine wakes

An assessment of the accuracy of the LiSBOA in the calculation of mean wind speed and turbulence intensity is now provided for LiDAR measurements performed during the occurrence of wake interactions. To this aim, point-wise measurements provided by the nacelle-mounted anemometers and saved in the SCADA data of four closely spaced Mitsubishi wind turbines, roughly aligned with the wind direction, are compared with the statistics obtained from the post-processing of the LiDAR data with the LiSBOA.

Figure 14 reports a satellite image of the site of this experiment. The tests were performed during the occurrence of a nearly steady north-easterly wind ($U_\infty \sim 8$ m s^{-1}) from 9 pm to 1 am local time (~~$T = 4h$~~$T = 4$ h) in the night between 5 and 6
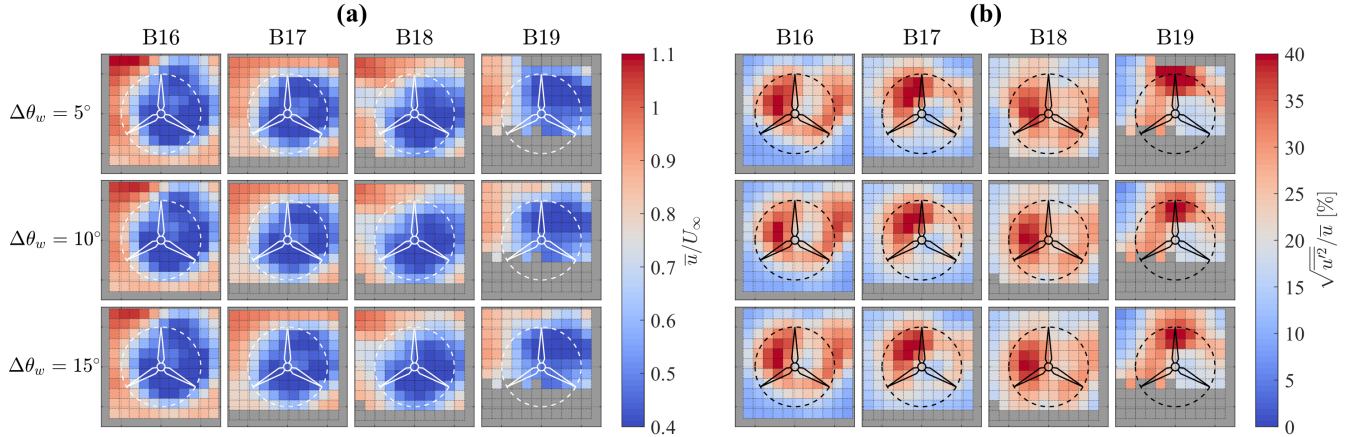
Figure 13. Fields reconstructed adopting several $\Delta\theta_w$ values and sampled at $x/D \sim 1.3$ downstream of turbines B16, B17, B18 and B19: (a) mean streamwise velocity; (b) streamwise turbulence intensity.
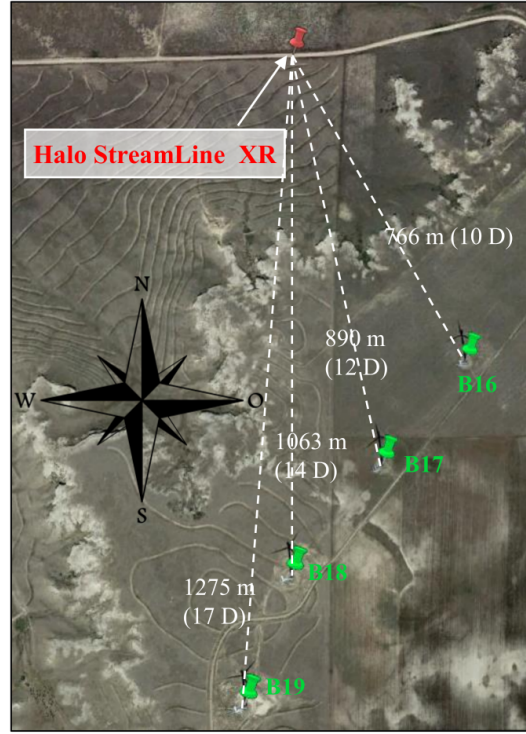
Figure 14. Satellite map of the site for the deployment of the Windcube 200S LiDAR, including the four Mitsubishi wind turbines under investigation. Source: Google Maps.

255   September 2018. This wind condition created a good alignment of the wakes emitted by the turbines F01 to F04. The aerosol conditions allowed us to run the Windcube 200S LiDAR with a gate length of 50 m and an accumulation time of 0.5 s. The LiDAR is located at a distance of about $25D$ from the wind turbine F04, which is the most downstream turbine for that specific wind condition, while the average streamwise spacing between the turbines is $3.6D$. The velocity and turbulence intensity fields are reconstructed over a horizontal plane including only points within the vertical range spanning from the bottom- to

260   top-tip of the turbine rotors. The 2D reconstruction here adopted implies that a uniform weight is applied for points displaced at different z, which means the reconstructed statistics represent time and vertically-averaged fields. This 2D approach is deemed convenient for the comparison with point-wise measurements recorded by the SCADA through nacelle-mounted instruments representing an average of the wind characteristics over the rotor.

     The region of interest was probed through a volumetric scan consisting of three PPI scans with elevation angles $\beta =$

265    $2.1°, 2.6°$, and $3.3°$. The fundamental half-wavelengths were selected as $\Delta n_{0,x} = 2.25D$, $\Delta n_{0,y} = 0.75D$. According to the previous cases, the integral time-scale was estimated to be $\tau U_\infty/D = 0.4$ ($\tau \sim 3$ s). The characteristic velocity standard deviation was set to $\sqrt{\overline{u'^2}} = 0.2\,U_\infty$. The value of the associated turbulence intensity is higher than that used for non-overlapping

wakes to account for the turbulence build-up, which is known to occur for turbines operating experiencing wake interactions (Chamorro and Porté-Agel, 2011; Iungo et al., 2013a).

270   The incoming wind is characterized by averaging measurements collected from all the anemometers and wind vanes installed on both met towers, which are located 12 km and 10.4 km away from the leading turbine F01 (Fig. 15). The Obukhov length is calculated from both sonic anemometers indicating a stable stratification regime. The SCADA data exhibits the typical signature of multiple wake interactions with reduced wind speed and power for downstream turbines, while turbulence intensity is enhanced, in particular for the F02 and F04 wind turbines.

275   The optimal design of the LiDAR scan is performed considering six values of $\Delta\theta$ and four values of σ. The obtained Pareto front is shown in Fig. 16, which indicates $\Delta\theta = 0.5°$ and $\sigma = 1/3, 1/4$ or $1/6$ as the optimal scanning parameters. The equivalent velocity retrieved by the LiDAR is made non-dimensional with the freestream velocity provided by the met-towers. The wind direction range is set to $\Delta\theta_w = 10°$, resulting in a total measuring period of 150 minutes. Data points lying above the top-tip or below the bottom-tip heights are excluded for this data analysis. The dynamic filter technique is used to reject

280   corrupted LiDAR data, producing a total of 544,000 quality-controlled LiDAR samples over 1,327,000 collected LiDAR data within the selected wind-direction range.

The LiSBOA is carried out on a grid with resolution $\boldsymbol{dx = 0.25\Delta n_0}$, using the combination smoothing parameters - number of iterations $\sigma = 1/6$ - $m = 1$, which is, among the allowable combinations, the one providing the largest response of the higher-order moments. The obtained velocity and turbulence intensity fields over the horizontal plane at hub height are displayed in

285   Fig. 17. The velocity deficit of F02 appears slightly larger than that detected behind the unwaked turbine F01, which is most probably due to the wake superimposition. An even deeper velocity deficit can be observed behind F03, which operates in a partially waked condition for this specific wind direction. Downstream of the third turbine, the wake deficit build-up saturates,
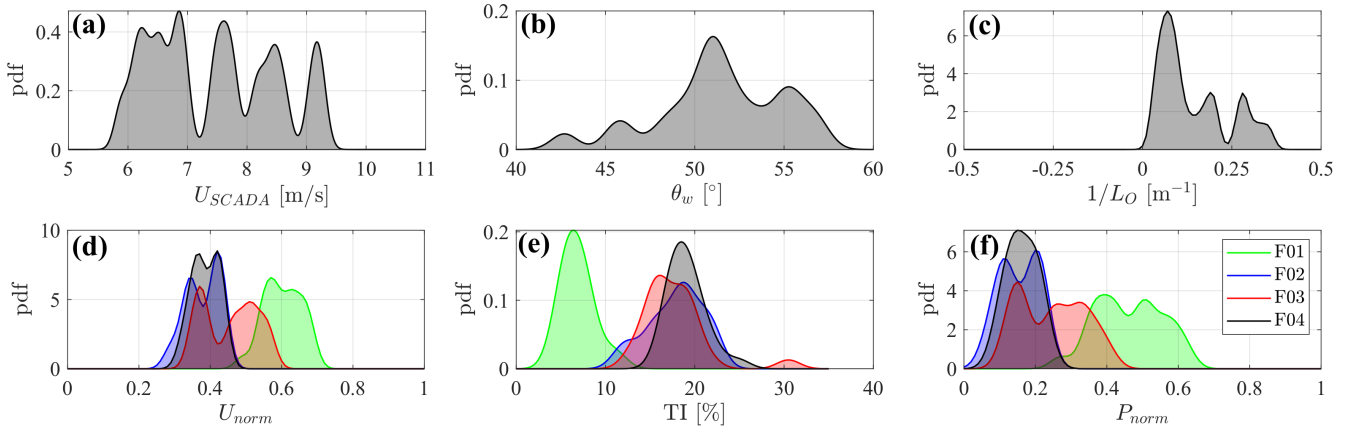
Figure 15. Probability density functions of the met and SCADA data recorded from 21:00 to 1:00 MDT on the night between September 5 and 6 2018: **(a)** wind speed from met-towers; **(b)** wind direction from met-towers; **(c)** inverse Obukhov length from our sonic anemometers; **(d)** normalized wind speed from SCADA; **(e)** turbulence intensity from SCADA; **(f)** normalized power from SCADA.
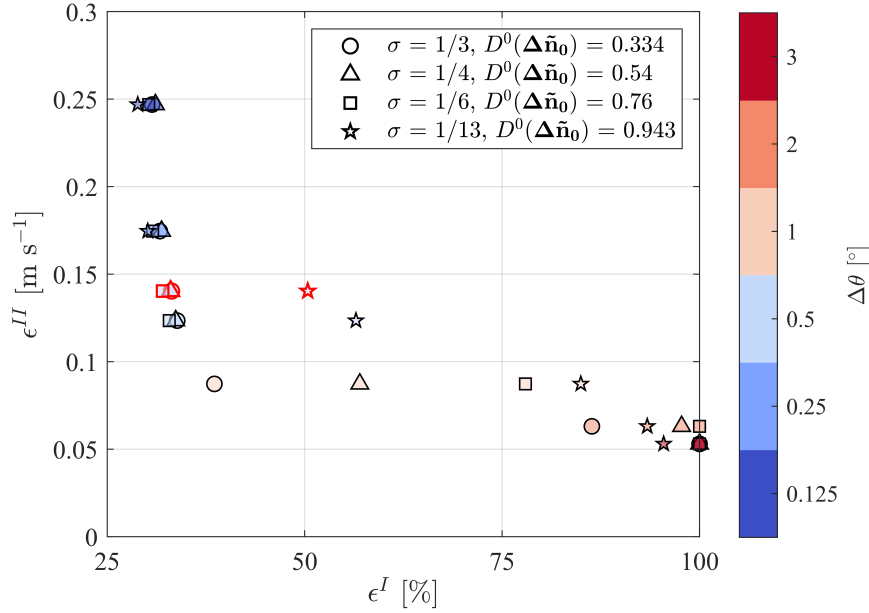
Figure 16. Pareto front for the design of the optimal LiDAR scan for the reconstruction of the wakes statistics for the turbine F01-F04. The markers highlighted in red represent the actual LiDAR data after ~~the~~ quality control.

confirming results from previous studies on close wake interactions (Barthelmie et al., 2010; Chamorro and Porté-Agel, 2011). Finally, the relatively fast recovery of the wake of the trailing turbine, F04, can be ascribed to the enhanced mixing due to the wake-generated turbulence. Indeed, Fig. 17b shows significant wake-generated turbulence increasing past the leading turbine that reaching its maximum at a distance of $1D$ downstream of the rotor of F03. Interestingly, wake-generated turbulence is concentrated on the sides of the wake of F01, which experiences undisturbed flow, while it spreads among the whole wake region for the downstream turbines. This feature might be related to the presence of coherent wake vorticity structures in the near wake of turbine F01 (Iungo et al., 2013a; Viola et al., 2014; Ashton et al., 2016), while further downstream, the perturbed inflow promotes the breakdown of such coherent structures leading to more homogeneous turbulence. Finally, the large velocity deficit/high turbulence detected in the wake of F03 may be a consequence of the mentioned partial wake interaction, which exposes the rotor to a non-homogeneous flow resulting in a severely off-design operation.

From a more quantitative standpoint, the incoming wind conditions experienced by each turbine are characterized to perform a direct comparison with the nacelle-anemometer data. To this aim, the mean velocity and turbulence intensity profiles are extracted from the LiDAR statistics at a distance of $1D$ upstream of the rotors over a segment spanning the whole rotor diameter. The sampling location is chosen based on previous studies (Politis et al., 2012; Hirth et al., 2015), since $1D$ is generally considered the minimum distance upstream of the rotor where the influence of the induction zone can be neglected for normal operative conditions. The averaged values of $\overline{u}/U_\infty$ and $\sqrt{\overline{u'^2}}/\overline{u}$ of each upstream profile are then used for the comparison with the respective values recorded through the SCADA.
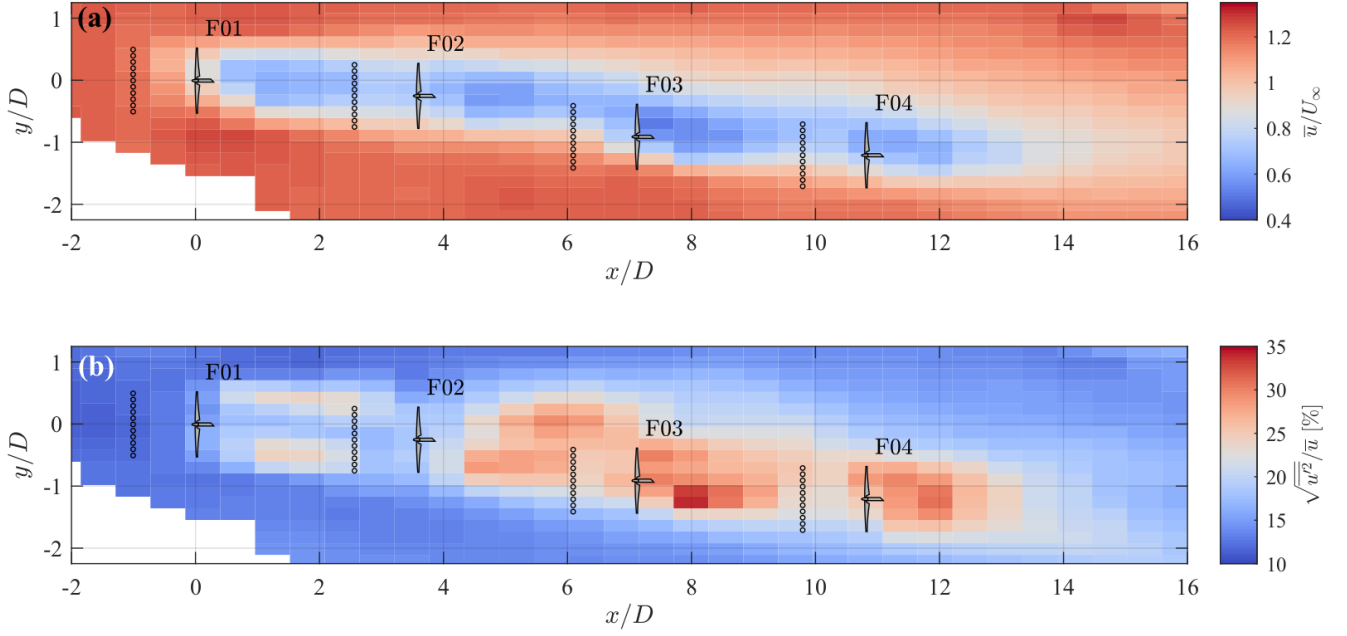
Figure 17. Velocity statistics of the wakes generated by the turbines F01-F04 reconstructed over the horizontal plane at hub height: **(a)** mean streamwise velocity; **(b)** streamwise turbulence intensity. The black dots indicate the sampling locations used for the estimation of the incoming flow for the respective turbine.

A well-posed comparison of the wind statistics obtained from the LiSBOA, the SCADA and met-data requires two important elements: firstly, the statistical moments compared have to be equivalent; secondly, both the LiSBOA and the SCADA data must be representative of the freestream conditions experienced by each turbine.

Regarding the first issue, the mean field obtained through the LiSBOA, $\overline{u}$, can be expressed as:

$$\left\langle \frac{u}{U_\infty} \right\rangle_T = \left\langle \left\langle \frac{u}{U_\infty} \right\rangle_{\hat{T}} \right\rangle_T \sim \left\langle \frac{U_{\text{SCADA}}}{U_{\text{met}}} \right\rangle_T \tag{3}$$

where $\langle . \rangle_T$ is the average calculated over the whole sampling period of 150 minutes, while $\langle . \rangle_{\hat{T}}$ is the 10-minute average performed by the SCADA and the met-tower acquisition system. U_{SCADA} and U_{met} are the 10-minute averaged velocities recorded from the SCADA and met-tower, respectively, while the symbol $\sim$ indicates statistical equivalence.

Similarly, for the comparison between the velocity variance calculated through the LiSBOA and the respective values recorded through the SCADA, we have the following relationship:

$$\left\langle \frac{u'^2}{U_\infty^2} \right\rangle_T = \left\langle \left\langle \frac{\hat{u}'^2}{U_\infty^2} \right\rangle_{\hat{T}} \right\rangle_T + \left\langle \left\langle \frac{u}{U_\infty} \right\rangle_{\hat{T}}^2 \right\rangle_T - \left\langle \left\langle \frac{u}{U_\infty} \right\rangle_{\hat{T}} \right\rangle_T^2 \sim \left\langle \frac{U_{\text{SD, SCADA}}^2}{U_{\text{met}}^2} \right\rangle_T + \left\langle \frac{U_{\text{SCADA}}^2}{U_{\text{met}}^2} \right\rangle_T - \left\langle \frac{U_{\text{SCADA}}}{U_{\text{met}}} \right\rangle_T^2 \tag{4}$$

where u' and $\hat{u}'$ are the velocity fluctuations with zero mean calculated over the period T and $\hat{T}$, respectively. The parameter $U_{\text{SD, SCADA}}^2$ is the velocity variance recorded by the SCADA over the period $\hat{T}$ of 10 minutes.

To ensure that the SCADA mean and standard deviation of velocity are representative of the undisturbed wind conditions at each rotor, these velocity statistics are corrected for the flow distortion induced by the turbine through appropriate nacelle transfer functions (NTF), which converts the velocity statistics measured at the nacelle of a wind turbine to the corresponding freestream values measured from a met-tower located nearby. The IEC standard 61400-12-2 (International Electrotechnical Commission, 61400-12-2, 2013) prescribes to calculate the NTF from the bin average with bin size 0.5 m s^{-1} of the velocity measured by a reference anemometer as a function of the nacelle wind speed. In the present work, besides correcting the mean wind speed as indicated by the IEC standards, a linear correction of the wind speed standard deviation is also applied, as suggested by Argyle et al. (2018). We adopted as reference anemometer that installed at 69 m above the ground on met tower #2. The SCADA data of Mitsubishi turbines H05 and H06, both falling in the range of distances from the met-tower recommended by the IEC 61400-12-1 (International Electrotechnical Commission 61400-12-1, 2017), are used. Only the unwaked wind sectors calculated based on the same standard are considered. The described layout is shown in Fig. 18, while Fig. 19 shows the result of this analysis. There is a high correlation between the velocity measured by the met-tower and the nacelle-mounted anemometer ($\rho = 0.976$). Nevertheless, the NTF of the velocity reveals consistently lower values occurring at the nacelle compared to the met-tower, with a peak at 20 m s^{-1}. Concerning the standard deviation of velocity, the agreement between SCADA and met-tower data is significantly lower ($\rho = 0.828$), yet a linear correction can be still calculated with acceptable significance (error on slope and intercept are 0.0038 and 0.0034 with 95% confidence).
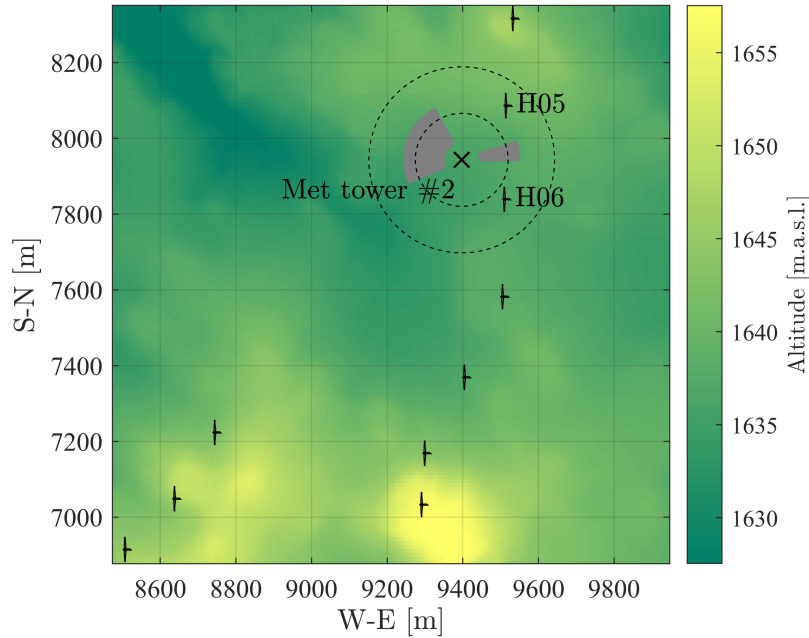
Figure 18. Met-tower and turbines selected for the nacelle transfer function estimation. The directions highlighted in grey represent the valid wind sectors unaffected by turbine wake interactions. The dashed circles bound the allowed range of distances from the tower in compliance with IEC standard 61400-12-1 (International Electrotechnical Commission 61400-12-1, 2017).
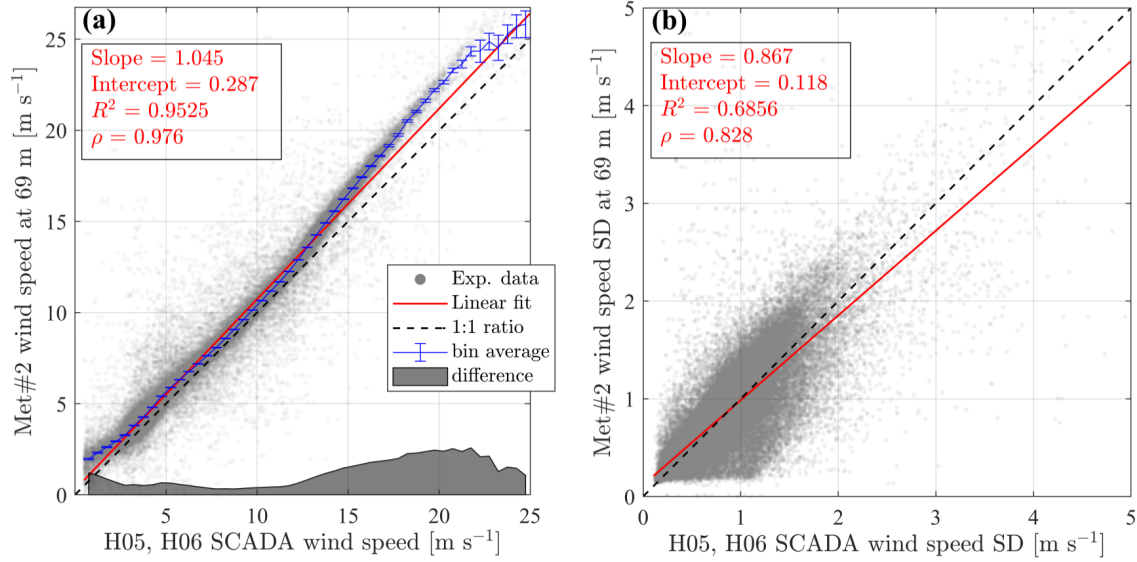
Figure 19. Nacelle transfer function for mean **(a)** and standard deviation **(b)** of wind speed. The error bars represent the standard error on the mean with 95% confidence level.

The results of the comparison between LiSBOA and SCADA are provided in Fig. 20. The mean velocity is accurately captured and confirms that F02 and F04 are the turbines mainly affected by the upstream wakes. The slightly higher momentum impinging F03 is mostly due to the imperfect alignment of that rotor with the upstream turbine wakes, which creates a condition of partial-wake interaction. A slightly larger discrepancy between LiSBOA and SCADA data is observed for the turbulence intensity, with a maximum difference of $\sim 3\%$ for F03. Nonetheless, the main trend is well reproduced and the overall agreement is satisfactory. The observed difference in turbulence intensity can be related to several factors, such as turbulence damping due to the LiDAR measuring process and LiSBOA calculations, the accuracy of the NTF, estimate of the streamwise velocity from the LiDAR radial velocity or vertical dispersive stresses.

The effect of the sampling location upstream of the turbines in the LiSBOA field is investigated by quantifying the discrepancy of the LiSBOA statistics with respect to the reference SCADA values for all the turbines through the 95-th percentile of the absolute error, AE_{95}. Figure 21 shows AE_{95} as a function of the distance upstream where the incoming flow is extracted from the LiSBOA statistics. For the mean velocity, it is confirmed that the value suggested by the literature ($x = -1D$) is sufficiently far from the rotor to limit the effects of the induction zone on the definition of the reference freestream velocity. Furthermore, the rotor thrust does not seem to have noticeable effects on the incoming turbulence, being the induction zone essentially devoid of significant turbulent fluctuations due to the loads of the turbine blades. The discrepancy between the turbulence intensity retrieved through LiSBOA and SCADA steeply increases for sampling locations further than $2D$ from the rotor.
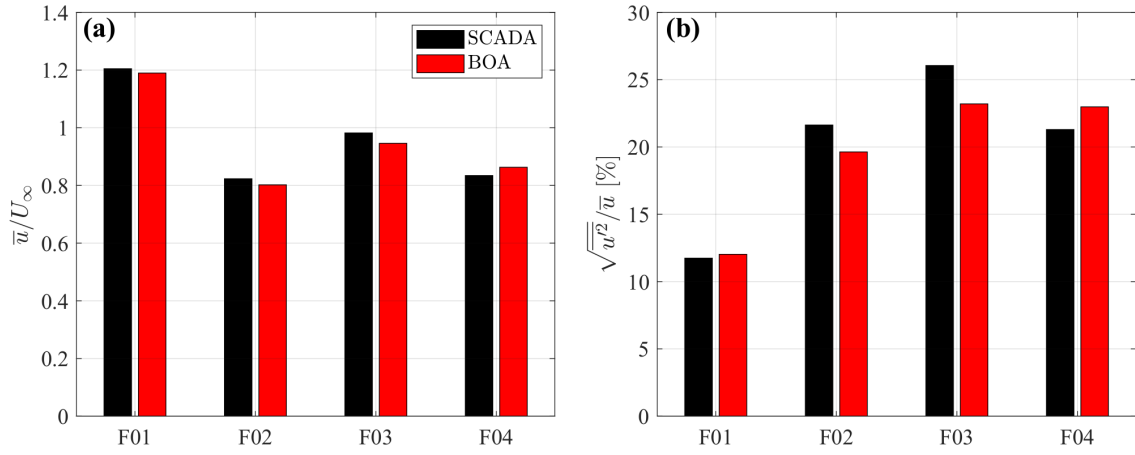
Figure 20. Comparison between LiSBOA and SCADA wind statistics for a case with wake interactions: **(a)** mean streamwise velocity normalized by freestream velocity; **(b)** streamwise turbulence intensity.
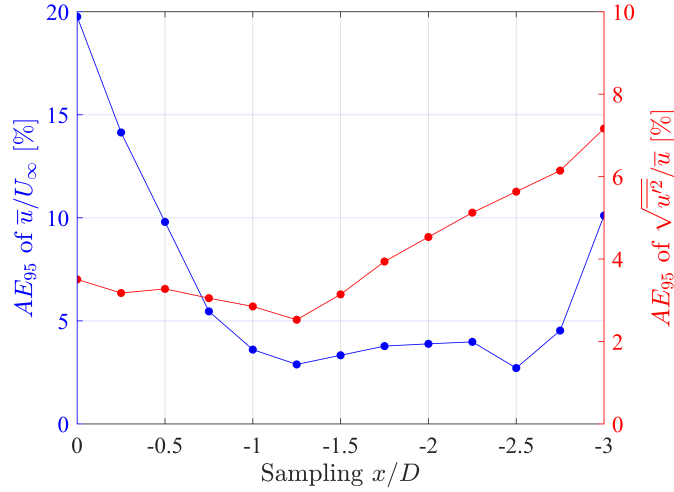
Figure 21. AE_{95} of mean velocity and turbulence intensity for F01-F04 as a function of the upstream sampling location of the LiSBOA fields.

Summarizing, the satisfactory agreement between LiSBOA and SCADA data achieved in the present study indicates the proposed procedure as a promising candidate for wind resource assessment, especially for complex terrains, and investigations of the intra-wind-farm flow.

5   Conclusions

355   The LiDAR Statistical Barnes Objective Analysis (LiSBOA) has been applied to two different cases of wind turbine wakes to estimate the optimal ~~LiDAR scanning strategy~~ azimuthal step of the LiDAR and retrieve mean velocity and turbulence intensity fields.

First, the LiSBOA has been used to process real LiDAR data collected for a utility-scale wind farm. For the first test case, the statistics of the wakes of four non-interacting 1.5-MW turbines placed at the brink of an escarpment have been reconstructed.

360   The optimal ~~LiDAR scanning strategy~~ azimuthal resolution of the LiDAR scan has been selected through the LiSBOA, while the mean velocity and turbulence intensity fields retrieved through the LiSBOA have offered a detailed insight of the wake morphology. Furthermore, a sensitivity analysis of the wind direction range has confirmed the robustness of the data selection and quality control methods.

Subsequently, the complex velocity field arising from the interaction of four 1-MW turbines has been analyzed by calculating

365   first and second-order moments on the horizontal plane. The mean velocity and turbulence intensity extracted $1D$ upstream of the rotors have agreed well with the values provided by the nacelle anemometers, with maximum discrepancies as low as 3% of the undisturbed wind speed for the mean velocity and 3% (in absolute terms) for the turbulence intensity.

The applications of the LiSBOA discussed in this work aims to showcase the potential of the proposed procedure for the optimal design of LiDAR scans and to provide guidelines for the utilization of the LiSBOA for the analysis of LiDAR data.

370   Two noticeable advantages of the LiSBOA arise from the present work: first, once the wavelengths of interest and the LiDAR basic ~~setup~~ scanning parameters dictated by the atmospheric conditions and target position are selected, the LiSBOA allows a systematic and effective ~~design of LiDAR scans~~ optimization of the azimuthal resolution, which includes all the essential information of the flow under investigation and the LiDARs used. This feature can be of interest, especially when planning field experiments that involve multiple LiDARs, complex topography, or articulated turbine configurations. In such situations,

375   the use of the proposed quantitative and comprehensive scan design approach may be beneficial to narrow down a great deal of arbitrariness and uncertainty associated with ~~the~~ campaign planning. Second, the LiSBOA offers complete control over the response of the spatial wavelengths of the velocity field for the statistical moments with various order. This feature is crucial when dealing with turbulent and multi-scale flows because it allows extracting meaningful information from the flow while filtering out small-scale variability.

380   *Code availability.* The LiSBOA algorithm is implemented in a publicly available code which can be downloaded at the following URL: https://www.utdallas.edu/windflux/software-datasets/.

Author contributions. SL and GVI developed the LiSBOA and prepared the manuscript. The LiDAR data were generated as a team effort including contributions from all three authors. SL implemented the LiSBOA in a Matlab code and performed data analysis under the supervision of GVI.

385   *Competing interests.*   No competing interests are present.

Acknowledgements.   This research has been funded by a grant from the National Science Foundation CBET Fluid Dynamics, award number 1705837. This material is based upon work supported by the National Science Foundation under grant IIP-1362022 (Collaborative Research: I/UCRC for Wind Energy, Science, Technology, and Research) and from the WindSTAR I/UCRC Members: Aquanis, Inc., EDP Renewables, Bachmann Electronic Corp., GE Energy, Huntsman, Hexion, Leeward Asset Management, LLC, Pattern Energy, EPRI, LM Wind, Texas

390   Wind Tower and TPI Composites. Any opinions, findings, and conclusions or recommendations expressed in this material are those of the authors and do not necessarily reflect the views of the sponsors. Texas Advanced Computing Center is acknowledged for providing computational resources. The authors acknowledge the support of the owners and operator of the wind farm, and the landowners of the test site.

References

Aitken, M. L. and Lundquist, J. K.: Utility-Scale Wind Turbine Wake Characterization Using Nacelle-Based Long-Range Scanning Lidar, J. Atmos. Ocean. Tech., 31, 1529–1539, https://doi.org/10.1175/JTECH-D-13-00218.1, 2014.

Argyle, P., Watson, S., Montavon, C., Jones, I., and Smith, M.: Modelling turbulence intensity within a large offshore wind farm, Wind Energy, 21, 1329–1343, https://doi.org/10.1002/we.2257, 2018.

Ashton, R., Iungo, G. V., Viola, F., Gallaire, F., and Camarri, S.: Hub vortex instability within wind turbine wakes : Effects of wind turbulence, loading conditions and blade aerodynamics, Physical Review Fluids, 1, 073 603, https://doi.org/10.1103/PhysRevFluids.1.073603, 2016.

Aubrun, S., Torres Garcia, E., Boquet, M., Coupiac, O., and Girard, N.: Wind turbine wake tracking and its correlations with wind turbine monitoring sensors. Preliminary results, Journal of Physics: Conference Series, 753, 032 003, https://doi.org/10.1088/1742-6596/753/3/032003, https://doi.org/10.1088, 2016.

Barnes, S. L.: A Technique for Maximizing Details in Numerical Weather Map Analysis, J. Appl. Meteorol., 3, 396–409, https://doi.org/10.1175/1520-0450(1964)003<0396:ATFMDI>2.0.CO;2, 1964.

Barthelmie, R. J., Hansen, K., Frandsen, S. T., Rathmann, O., Schepers, J. G., Schlez, W., Phillips, J., Rados, K., Zervos, A., Politis, E. S., and Chaviaropoulos, P. K.: Modelling and Measuring Flow and Wind Turbine Wakes in Large Wind Farms Offshore, Wind Energy, 12, 431–444, https://doi.org/10.1002/we.348, 2009.

Barthelmie, R. J., Pryor, S. C., Frandsen, S. T., Hansen, K. S., Schepers, J. G., Rados, K., Schelz, W., Neubert, A., Jensen, L. E., and Neckelmann, S.: Quantifying the Impact of Wind Turbine Wakes on Power Output at Offshore Wind Farms, J. Atmos. Ocean. Tech., pp. 1302–1317, https://doi.org/10.1175/2010JTECHA1398.1, 2010.

Beck, H. and Kühn, M.: Dynamic Data Filtering of Long-Range Doppler LiDAR Wind Speed Measurements, Remote Sens.-Basel, 9, 561, 2017.

Berg, J., Mann, J., Bechmann, A., Courtney, M. S., and Jørgensen, H. E.: The Bolund Experiment. Part I : Flow Over a Steep, Three-dimensional Hill, Bound.-Lay. Meteorol., pp. 219–243, https://doi.org/10.1007/s10546-011-9636-y, 2011.

Bingöl, F., Mann, J., and Larsen, G. C.: Light detection and ranging measurements of wake dynamics. Part I: one-dimensional scanning, Wind Energy, 13, 51–61, https://doi.org/10.1002/we.352, 2010.

Bodini, N., Zardi, D., and Lundquist, J. K.: Three-dimensional structure of wind turbine wakes as measured by scanning lidar, Atmos. Meas. Tech., 10, 2881–2896, https://doi.org/10.5194/amt-10-2881-2017, 2017.

Bromm, M., Rott, A., Beck, H., Vollmer, L., Steinfeld, G., and Kühn, M.: Field investigation on the influence of yaw misalignment on the propagation of wind turbine wakes, Wind Energy, 21, 1011–1028, https://doi.org/10.1002/we.2210, 2018.

Carbajo Fuertes, F., , Markfort, D., C., and Porté-Agel, F.: Wind Turbine Wake Characterization with Nacelle-Mounted Wind Lidars for Analytical Wake Model Validation, Remote Sens.-Basel, 10, https://doi.org/10.3390/rs10050668, 2018.

Chamorro, L. P. and Porté-Agel, F.: Turbulent flow inside and above a wind farm: A wind-tunnel study, Energies, 4, 1916–1936, https://doi.org/10.3390/en4111916, 2011.

Clifton, A., Clive, P., Gottschall, J., Schlipf, D., Simley, E., Simmons, L., Stein, D., Trabucchi, D., Vasiljevic, N., and Würth, I.: IEA Wind Task 32: Wind lidar identifying and mitigating barriers to the adoption of wind lidar, Remote Sens.-Basel, 10, 1–22, https://doi.org/10.3390/rs10030406, 2018.

Clive, P. J. M., Dinwoodie, I., and Quail, F.: Direct measurement of wind turbine wakes using Remote Sens.-Basel, Proceedings of the EWEA, 2011.

El-Asha, S., Zhan, L., and Iungo, G. V.: Quantification of power losses due to wind turbine wake interactions through SCADA, meteorological and wind LiDAR data, Wind Energy, 20, 1823–1839, https://doi.org/10.1002/we.2123, 2017.

España, G., Aubrun, S., Loyer, S., and Devinant, P.: Spatial study of the wake meandering using modelled wind turbines in a wind tunnel, Wind Energy, 14, 923–937, https://doi.org/10.1002/we, http://onlinelibrary.wiley.com/doi/10.1002/we.1608/full, 2011.

435   Fernando, H. J. S., Mann, J., Palma, J. M. L. M., Lundquist, J. K., Barthelmie, R. J., Belo-Pereira, M., Brown, W., Chow, F. K., and Gerz, T., e. a.: Peering into microscale details of mountain winds, B. Am. Meteorol. Soc., 100, 799–820, https://doi.org/10.1175/BAMS-D-17-0227.1, 2019.

Floors, R., Peña, A., Lea, G., Vasiljević, N., Simon, E., and Courtney, M.: The RUNE experiment-A database of remote-sensing observations of near-shore winds, Remote Sens.-Basel, 8, https://doi.org/10.3390/rs8110884, 2016.

440   Fuertes Carbajo, F. and Porté-Agel, F.: Using a Virtual Lidar Approach to Assess the Accuracy of the Volumetric Reconstruction of a Wind Turbine Wake, Remote Sens.-Basel, 10, https://doi.org/10.3390/rs10050721, 2018.

Garcia, E. T., Aubrun, S., Boquet, M., Royer, P., Coupiac, O., and Girard, N.: Wake meandering and its relationship with the incoming wind characteristics: a statistical approach applied to long-term on-field observations, Journal of Physics: Conference Series, 854, 012 045, https://doi.org/10.1088/1742-6596/854/1/012045, 2017.

445   Gottschall, J., Catalano, E., M., D., and Witha, B.: The NEWA Ferry Lidar Experiment: Measuring mesoscale winds in the Southern Baltic Sea, Remote Sens.-Basel, 10, 1–13, https://doi.org/10.3390/rs10101620, 2018.

Hansen, K. S. and Barthelmie, R.: The impact of atmospheric stability on Horn Rev wind farm, Wind Energy, 17, 657–669, https://doi.org/10.1002/we, http://onlinelibrary.wiley.com/doi/10.1002/we.1608/full, 2014.

Hirth, B. D., Schroeder, J. L., Gunter, W. S., and Guynes, J. G.: Coupling Doppler radar-derived wind maps with operational turbine data to

450   document wind farm complex flows, Wind Energy, 18, 529–540, https://doi.org/10.1002/we, 2015.

Hsuan, C. Y., Tasi, Y. S., Ke, J. H., Prahmana, R. A., Chen, K. J., and Lin, T. H.: Validation and measurements of floating LiDAR for nearshore wind resource assessment application, Energy Proced., 61, 1699–1702, https://doi.org/10.1016/j.egypro.2014.12.195, http://dx.doi.org/10.1016/j.egypro.2014.12.195, 2014.

International Electrotechnical Commission 61400-12-1: Wind energy generation systems – Part 12-1: Power performance measurements

455   of electricity producing wind turbines, International Standard 61400-12-2, International Electrotechnical Commission (IEC), Geneva, Switzerland, 2013., 2017.

International Electrotechnical Commission, 61400-12-2: Wind Turbine Generator Systems - Part 12-2: Power Performance of Electricity-Producing Wind Turbines Based on Nacelle Anemometry, International Standard 61400-12-2, International Electrotechnical Commission (IEC), Geneva, Switzerland, 2013., 2013.

460   Iungo, G. V. and Porté-Agel, F.: Volumetric Lidar Scanning of Wind Turbine Wakes under Convective and Neutral Atmospheric Stability Regimes, J. Atmos. Ocean. Tech., 31, 2035–2048, https://doi.org/10.1175/JTECH-D-13-00252.1, 2014.

Iungo, G. V., Viola, F., Camarri, S., Porté-Agel, F., and Gallaire, F.: Linear stability analysis of wind turbine wakes performed on wind tunnel measurements, J. Fluid Mech., 737, 499–526, https://doi.org/10.1017/jfm.2013.569, http://www.journals.cambridge.org/abstract{_}S0022112013005697, 2013a.

465   Iungo, G. V., Wu, Y., and Porté-Agel, F.: Field Measurements of Wind Turbine Wakes with Lidars, J. Atmos. Ocean. Tech., 30, 274–287, https://doi.org/10.1175/JTECH-D-12-00051.1, 2013b.

Iungo, G. V., Letizia, S., and Zhan, L.: Quantification of the axial induction exerted by utility-scale wind turbines by coupling LiDAR measurements and RANS simulations, Journal of Physics: Conference Series, 1037, https://doi.org/10.1088/1742-6596/1037/7/072023, 2018.

470 Karagali, I., Mann, J., Dellwik, E., and Vasiljević, N.: New European Wind Atlas: The Osterild balconies experiment, Journal of Physics: Conference Series, 1037, https://doi.org/10.1088/1742-6596/1037/5/052029, 2018.

Käsler, Y., S., R., Simmet, R., and Kühn, M.: Wake Measurements of a Multi-MW Wind Turbine with Coherent Long-Range Pulsed Doppler Wind Lidar, J. Atmos. Ocean. Tech., 27, 1529–1532, https://doi.org/10.1175/2010JTECHA1483.1, 2010.

Kim, D., Kim, T., Oh, G., Huh, J., and Ko, K.: A comparison of ground-based LiDAR and met mast wind measurements for wind resource
475 assessment over various terrain conditions, J. Wind Eng. Ind. Aerod., 158, 109–121, https://doi.org/10.1016/j.jweia.2016.09.011, http://dx.doi.org/10.1016/j.jweia.2016.09.011, 2016.

Koch, G. J., Beyon, J. Y., Cowen, L. J., Kavaya, M. J., and Grant, M. S.: Three-dimensional wind profiling of offshore wind energy areas with airborne Doppler lidar, J. Appl. Remote Sens., 8, 083 662, https://doi.org/10.1117/1.jrs.8.083662, 2014.

Krishnamurthy, R., Calhoun, R., Billings, B., and Doyle, J.: Wind turbulence estimates in a valley by coherent Doppler lidar, Meteorol. Appl.,
480 18, 361–371, https://doi.org/10.1002/met.263, 2011.

Krishnamurthy, R., Choukulkar, A., Calhoun, R., Fine, J., Oliver, A., and Barr, K. S.: Coherent Doppler lidar for wind farm characterization, Wind Energy, 16, 189–206, https://doi.org/10.1002/we, 2013.

Kumer, V. M., Reudera, J., Svardalc, B., Sætrec, C., and Eecen, P.: Characterisation of Single Wind Turbine Wakes with Static and Scanning WINTWEX-W LiDAR Data, Energy Proced., 80, 245 – 254, https://doi.org/https://doi.org/10.1016/j.egypro.2015.11.428, 12th Deep Sea
485 Offshore Wind R and D Conference, EERA DeepWind 2015, 2015.

Larsen, G. C., Madsen, H., Thomsen, K., and Larsen, T. J.: Wake meandering: A pragmatic approach, Wind Energy, 11, 377–395, https://doi.org/10.1002/we.267, 2008.

Letizia, S., Zhan, L., and Iungo, G. V.: LiSBOA: LiDAR Statistical Barnes Objective Analysis for optimal design of LiDAR scans and retrieval of wind statistics. Part I: Theoretical framework, Atmos. Meas. Tech. Discussions, 2020, 1–24, https://doi.org/10.5194/amt-
490 2020-227, https://amt.copernicus.org/preprints/amt-2020-227/, 2020.

Liu, Z., Barlow, J. F., Chan, P. W., Fung, J. C. H., Li, Y., Ren, C., Mak, H. W. L., and Ng, E.: A review of progress and applications of pulsed Doppler Wind LiDARs, Remote Sens.-Basel, 11, 1–47, https://doi.org/10.3390/rs11212522, 2019.

Machefaux, E., Larsen, G. C., Troldborg, N., Hansen, K. S., Angelou, N., Mikkelsen, T., and Mann, J.: Investigation of wake interaction using full-scale lidar measurements and large eddy simulation, Wind Energy, 19, 1535–1551, https://doi.org/10.1002/we.1936, 2015.

495 Machefaux, E., Larsen, G. C., Koblitz, T., Troldborg, N., Kelly, M. C., Chougule, A., Hansen, K. S., and Rodrigo, J. S.: An experimental and numerical study of the atmospheric stability impact on wind turbine wakes, Wind Energy, 19, 1785–1805, https://doi.org/10.1002/we.1950, 2016.

Menke, R., Vasiljevi, N., Mann, J., and Lundquist, J. K.: Characterization of flow recirculation zones at the Perdigão site using multi-lidar measurements, Atmos. Chem. Phys., 19, 2713–2723, https://doi.org/10.5194/acp-19-2713-2019, 2019.

500 Monin, A. S. and Obukhov, A. M.: Basic laws of turbulent mixing in the surface layer of the atmosphere, Tr. Akad. Nauk SSSR Geophiz. Inst., 24, 163–187, 1959.

Newman, J. F., Klein, P. M., Wharton, S., Sathe, A., Bonin, T. A., Chilson, P. B., and Muschinski, A.: Evaluation of three lidar scanning strategies for turbulence measurements, Atmos. Meas. Tech., 9, 1993–2013, https://doi.org/10.5194/amt-9-1993-2016, 2016.

Pauscher, L., Vasiljevic, N., Callies, D., Lea, G., Mann, J., Klaas, T., Hieronimus, J., Gottschall, J., Schwesig, A., Kühn, M., and
Courtney, M.: An inter-comparison study of multi- and DBS lidar measurements in complex terrain, Remote Sens.-Basel, 8,
https://doi.org/10.3390/rs8090782, 2016.

Pichugina, Y. L., Banta, R. M., Brewer, W. A., Sandberg, S. P., and Hardesty, R. M.: Doppler Lidar-based wind-profile measure-
ment system for offshore wind-energy and other marine boundary layer applications, J. Appl. Meteorol. Clim., 51, 327–349,
https://doi.org/10.1175/JAMC-D-11-040.1, 2012.

Politis, E. S., Prospathopoulos, J., Cabezon, D., and Hansen, K. S.: Modeling wake effects in large wind farms in complex terrain: the
problem, the methods and the issues, Wind Energy, 15, 161–182, https://doi.org/10.1002/we, 2012.

Risan, A., Lund, J. A., Chang, C. Y., and Sætran, L.: Wind in Complex Terrain - Lidar Measurements for Evaluation of CFD Simulations,
Remote Sens.-Basel, 10, 59, 2018.

Sanchez-Gomez, M. and Lundquist, J. K.: The effect of wind direction shear on turbine performance in a wind farm in central Iowa, Wind
Energy Science Discussions, pp. 1–23, https://doi.org/10.5194/wes-2019-22, 2019.

Sathe, A., Mann, J., Gottschall, J., and Courtney, M. S.: Can Wind Lidars Measure Turbulence?, J. Atmos. Ocean. Tech., 28, 853–868,
https://doi.org/10.1175/JTECH-D-10-05004.1, 2011.

Shimada, S., Takeyama, Y., Kogaki, T., Ohsawa, T., and Nakamura, S.: Investigation of the fetch effect using onshore and offshore vertical
LiDAR devices, Remote Sens.-Basel, 10, https://doi.org/10.3390/rs10091408, 2018.

Sommerfeld, M., Crawford, C., Monahan, A., and Bastigkeit, I.: LiDAR-based characterization of mid-altitude wind conditions for air-
borne wind energy systems, Wind Energy, p. we.2343, https://doi.org/10.1002/we.2343, https://onlinelibrary.wiley.com/doi/abs/10.1002/
we.2343, 2019.

Trujillo, J. J., F., B., Larsen, G. C., Mann, J., and Kühn, M.: Light detection and ranging measurements of wake dynamics. Part II: two-
dimensional scanning, Wind Energy, 14, 61–75, https://doi.org/10.1002/we.402, 2011.

Trujillo, J. J., Seifert, J. K., Würth, I., Schlipf, D., and Kühn, M.: Full-field assessment of wind turbine near-wake deviation in relation to
yaw misalignment, Wind Energy Science, 1, 41–53, https://doi.org/10.5194/wes-1-41-2016, 2016.

Van Dooren, M. F., Trabucchi, D., and Kühn, M.: A Methodology for the Reconstruction of 2D Horizontal Wind Fields of Wind Turbine
Wakes Based on Dual-Doppler Lidar Measurements, Remote Sens.-Basel, 8, https://doi.org/10.3390/rs8100809, 2016.

Vasiljević, N., Palma, J. M. L. M., Angelou, N., Matos, J. C., Menke, R., Lea, G., Mann, J., Courtney, M., Ribeiro, L. F., and C., G. V.
M. M. G.: Perdigão 2015 : Methodology for atmospheric multi-Doppler lidar experiments Perdigão 2015 : methodology for atmospheric
multi-Doppler lidar experiments, Atmos. Meas. Tech., 10, 3463–3483, https://doi.org/10.5194/amt-10-3463-2017, 2017.

Veers, P., Dykes, K., Lantz, E., Barth, S., Bottasso, C. L., Carlson, O., Clifton, A., Green, J., Green, P., Holttinen, H., Laird, D., Lehtomäki,
V., Lundquist, J. K., Manwell, J., Marquis, M., Meneveau, C., Moriarty, P., Munduate, X., Muskulus, M., Naughton, J., Pao, L., Paquette,
J., Peinke, J., Robertson, A., Rodrigo, J. S., Sempreviva, A. M., Smith, J. C., Tuohy, A., and Wiser, R.: Grand challenges in the science of
wind energy, Science, 366, https://doi.org/10.1126/science.aau2027, 2019.

Viola, F., Iungo, G. V., Camarri, S., Porté-Agel, F., and Gallaire, F.: Prediction of the hub vortex instability in a wind turbine wake: Stability
analysis with eddy-viscosity models calibrated on wind tunnel data, J. Fluid Mech., 750, R1, https://doi.org/10.1017/jfm.2014.263, 2014.

Viselli, A., Filippelli, M., Pettigrew, N., Dagher, H., and Faessler, N.: Validation of the first LiDAR wind resource assessment buoy system
offshore the Northeast United States, Wind Energy, p. we.2387, https://doi.org/10.1002/we.2387, https://onlinelibrary.wiley.com/doi/abs/
10.1002/we.2387, 2019.

Wang, H. and Barthelmie, R. J.: Wind turbine wake detection with a single Doppler wind lidar, Journal of Physics: Conference Series, 625, 012 017, https://doi.org/10.1088/1742-6596/625/1/012017, 2015.

Zhan, L., Letizia, S., and Iungo, G. V.: LiDAR measurements for an onshore wind farm: Wake variability for different incoming wind speeds and atmospheric stability regimes, Wind Energy, pp. 1–27, https://doi.org/10.1002/we.2430, 2019.

545 Zhan, L., Letizia, S., and Iungo, G. V.: Wind LiDAR Measurements of Wind Turbine Wakes Evolving over Flat and Complex Terrains: Ensemble Statistics of the Velocity Field, Journal of Physics: Conference Series, 1452, https://doi.org/10.1088/1742-6596/1452/1/012077, 2020.